



Microstructure and corrosion behavior of duplex stainless steel electron beam welded joint

Jastej Singh^{1,*}  and A. S. Shahi¹

¹Department of Mechanical Engineering, Sant Longowal Institute of Engineering & Technology (Deemed-to-be University), Sangrur 148106, Punjab, India

Received: 8 January 2022

Accepted: 15 April 2022

Published online:

10 May 2022

© The Author(s), under exclusive licence to Springer Science+Business Media, LLC, part of Springer Nature 2022

ABSTRACT

The aim of the present work was to carry out detailed corrosion and microstructural studies on exclusively the fusion zone/weld metal region of 2205 duplex stainless steel (DSS) electron beam (EB) welded joint in comparison with the base metal. Furthermore, the EB weld metal and DSS base metal were compared for their propensity to intermetallic precipitation during thermal aging based on their general and localized (pitting) corrosion characteristics in two different test solutions. Corrosion studies were performed using linear polarization resistance (LPR), potentiodynamic polarization (Tafel scan), electrochemical impedance spectroscopy (EIS), potentiodynamic anodic polarization, and cyclic potentiodynamic polarization (CPP) tests and were supported with microstructural characterization, ferrite content measurements, and X-ray diffraction (XRD) analysis. Microstructural heterogeneity existed within the weld metal which played an important role in affecting its pitting corrosion behavior. The general and pitting corrosion tendency of the weld metal was higher compared to the base metal, with the root region being the preferential site where pitting occurred within ferrite grains. Aging-induced σ -phase precipitation was detrimental to repassivation characteristics and decreased the resistance to pit growth for both weld metal and base metal. This study shows that in thick section autogenous EB DSS welds, the bottom/root region could be the potential site for preferential pitting corrosion attack due to its unfavorable microstructure, thus highlighting the importance of microstructural control in the root region while fabricating such welds.

Handling Editor: Catalin Croitoru.

Address correspondence to E-mail: jastejmech@gmail.com

Introduction

Duplex stainless steels (DSSs) are reliable engineering materials that are used mostly in aggressive service environments where the property to resist corrosion while exhibiting high mechanical strength is important. Their typical applications are in industries such as desalination, desulphurization, shipbuilding, chemical, petrochemical, offshore, pulp and paper, oil and gas, automotive, and architecture [1–3]. These alloys exhibit a superior combination of mechanical properties and corrosion resistance compared to austenitic and ferritic SSs, but their metallurgy in terms of processing and microstructural control is relatively more complex which makes their heat treatment and welding technically more challenging [4]. The primary problem associated with DSSs is their high propensity to formation of various deleterious phases such as α' , σ , χ , Cr-carbides, and Cr-nitrides, during high-temperature exposures in the range of 300–1000 °C. The precipitation of these phases may be caused by multiple factors such as application of welding, improper heat treatment procedures, plastic deformation, and aging during operational life, as a result of which degradation in localized corrosion resistance, toughness, and ductility can occur [5, 6].

The peculiarities of phase transformations, phase stability, and microstructural characteristics associated with DSSs during welding or high-temperature exposures play a key role in influencing their designated service life. In a review study on recurrent failures of DSSs, it was reported that most of the failures occurred in weld metal or heat-affected zone (HAZ) of welded components [4].

The industrial value of DSSs is dependent on the realization of welded joints. Extensive research has been carried out on the weldability of DSSs corresponding to different processes. Of particular importance has been the effect of weld thermal cycle-induced metallurgical transformations on corrosion properties of different regions of weldments. Yan et al. [7] observed in 2205 DSS gas tungsten arc weld joint that the dual-phase balance was disturbed although N_2 -supplemented shielding gas was used during welding, and HAZ exhibited the poorest pitting corrosion resistance. Zhang et al. [8] carried out investigations on microstructure and properties of DSS welds produced using gas tungsten arc welding

(GTAW) and flux-cored arc welding (FCAW) processes with different shielding gas compositions. Nitrogen addition in shielding gas was beneficial to the pitting resistance of GTA weld. The presence of inclusions in the weld metal of FCAW joint was detrimental to pitting corrosion resistance. In a study on tungsten inert gas (TIG) DSS S32101 welds, it was reported that an increase in welding heat input led to improvement in intergranular corrosion resistance which was due to an increase in austenite volume fraction in HAZ and decrease in Cr-nitride precipitates [9].

The effects of low energy input/high power density processes such as laser beam welding (LBW) and electron beam welding (EBW) on corrosion properties of DSSs are also reported, although limited in comparison with arc welding processes. Yang et al. [10] reported that the fusion zone of laser beam welded DSS UNS S31803 contained excessively high ferrite content besides Cr-nitride precipitates due to which the weld showed lower critical pitting temperature than the base metal. Similar observations related to adverse effects of unbalanced microstructure and precipitation of Cr-nitrides on pitting corrosion resistance of EB welded DSS are reported [11]. In a comparative study on EB-welded and GTA-welded 2205 DSS, it was observed that the EB weld exhibited higher pitting susceptibility than the GTA weld [12]. In a different study, the fusion zone size and extent of phase imbalance in microstructure were reported to influence the pitting corrosion behavior of EB DSS welds [13].

To lower safety risks for DSS components, the effects of thermal aging in causing degradation in corrosion resistance have been widely studied. Zeng et al. [14] studied the corrosion behavior of 2205 DSS aged at 850 °C. It was reported that σ was the primary phase that precipitated at 850 °C, and propagation of pitting took place along the Cr-depleted regions around the σ -phase. Magnabosco [15] studied phase transformations in UNS S31803 DSS isothermally aged between 700 and 900 °C and reported that higher kinetics of σ -phase formation occurred at 850 °C. Yongqiang et al. [16] while studying the pitting corrosion mechanism induced by σ -phase in three DSSs (SAF 2205, SAF 2507, and Z3CN20.09 M) concluded that pitting was not only due to the Cr-depleted zone itself but due to the extent of difference in Cr content between Cr-depleted zone and σ -phase.

Table 1 Chemical composition of 2205 DSS used in the present work

Element	Cr	C	Mo	Ni	V	Mn	Si	Ti	P	N	W	S	Nb	Fe
Wt %	22.338	0.026	3.12	5.429	0.058	1.585	0.524	0.006	0.028	0.2	0.002	0.010	0.031	Balance

The complex corrosion characteristics of DSSs are attributable to the presence of phase boundaries (which act as preferential sites for precipitation of secondary phases), and the partitioning of alloying elements, i.e., more N and Ni in austenite, and more Mo and Cr in ferrite. Furthermore, the type, size, and distribution of precipitates in microstructure also play an important role in the initiation of corrosion [17]. In a study on corrosion behavior of DSS 2205 aged at 850 °C, it was observed that the trend of charge transfer resistance from electrochemical impedance spectroscopy was not consistent with the corrosion current density parameter derived from the polarization curves [18]. Similarly, in a study on DSS FCA weldments with different Cr content, a discrepancy was reported between pitting potential values measured through polarization test and the sequence obtained by the pitting resistance equivalent number (PREN) of weaker phase [19].

It is clear from the literature survey that microstructural control during the welding of DSSs remains the key challenge to ensure satisfactory corrosion performance. Furthermore, the high propensity of DSSs to deleterious secondary phases upon exposure to elevated temperatures is another aspect due to which these alloys exhibit complex metallurgical behavior which is reflected in their corrosion characteristics. While abundant research works are available on microstructure and properties of DSS welds produced using conventional arc welding processes, relatively fewer studies have been reported on the combination of high-power density EBW process and DSS. Given the industrial importance of both, the EBW process and 2205 DSS (considered the real workhorse of the DSS family), and to address concerning issues related to weldability of this alloy, it is important to carry out a detailed investigation on the microstructure–corrosion property linkage for this alloy.

The present work was therefore primarily aimed at carrying out detailed microstructural and corrosion studies on exclusively the weld metal/fusion zone of EB welded 2205 DSS joint. Furthermore, the EB weld metal and DSS base metal were compared for their

propensity to intermetallic precipitation during thermal aging based on their general and localized (pitting) corrosion characteristics in two different test solutions. The findings of the present work would be relevant to the welding industry and would help in gaining insights into the welding behavior of DSS which can aid in attaining reliable welded fabrications. The study would be important from the service application viewpoint also as it attempted to demonstrate the propensity of weld metal and base metal to precipitation, and its effect on their corrosion characteristics which is an important aspect related to the structural integrity of DSS welds.

Experimental details

Material

The base material used in the present study was Type 2205 DSS (UNS S32205, EN 1.4462) in the form of flat-rolled plates of 18 mm thickness. Its chemical composition is presented in Table 1 [13].

Fabrication of EB weld joint

The edges of the base plates were cleaned and degreased with acetone before welding to remove any sources of contamination such as dust, rust, and scale which could contribute to weld defects later on. To achieve through-thickness penetration, a standard industrial welding procedure involving the use of a backing plate of 2205 DSS was adopted. The backing plate was incorporated in the assembly of the joint before carrying out EB welding [13]. After the evacuation of the chamber, EB welding was accomplished. Welding was performed in the autogenous mode, i.e., without the addition of filler material. A full-penetration close square butt weld joint was fabricated using a single weld pass. The details of the process parameters used are given in Table 2. After completion of welding, the chamber was de-evacuated and assembly was taken out followed by machining to remove the backing plate.

Table 2 EB welding parameters used in the present work

Beam current (mA)	Accelerating voltage (kV)	Welding/travel speed (mm/min.)	Focus current (mA)
90	150	600	2205

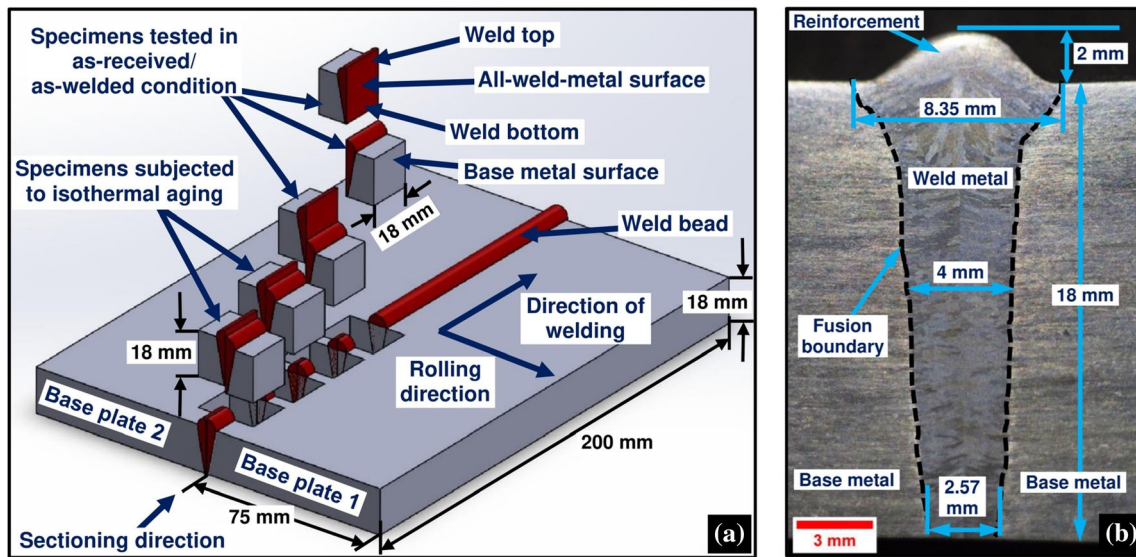


Figure 1 a Specimen sampling plan adopted in the present work and b macrostructure of the cross section of EB weld joint.

Specimen sampling and thermal aging treatment

Once the weld joint was fabricated, it was required to extract the all-weld-metal specimens, as it was intended to study the microstructure and corrosion behavior of exclusively the weld metal region. The EB weld was sectioned longitudinally using wire electrical discharge machining to reveal the surface comprising exclusively the fused weld metal. Figure 1a illustrates the specimen sampling plan adopted in the present work. The macrostructure of the weld cross section along with dimensions of bead across different regions is presented in Fig. 1b.

To induce secondary precipitation, half the number of specimens were isothermally aged in a microcontroller-based heating furnace at 850 °C for 2 h. After the set exposure time, the specimens were water-quenched to retain the phases formed in their microstructure due to the thermal exposure. The selection of aging treatment was based on the literature survey as discussed in the previous section [2, 3, 14–16, 18]. The details of different specimens are given in Table 3.

Table 3 Designation of different test specimens

Specimen	Description
BM0	Base metal (as-received condition)
WM0	Weld metal (as-welded condition)
BM1	Base metal (isothermally aged at 850 °C/2 h)
WM1	Weld metal (isothermally aged at 850 °C/2 h)

Microstructural, ferrite content, and XRD studies

The specimen preparation for metallography involved standard grinding and polishing procedures using SiC abrasive papers with grit sizes ranging from 100 to 2000. Microstructural studies were carried out using field-emission scanning electron microscopy (FE-SEM) supplemented with energy-dispersive X-ray spectroscopy (EDS). To reveal the microstructure, specimens were subjected to chemical etching in a solution comprising CuCl₂, HCl, and ethanol [13]. The ferrite content measurements were done using Fischer FMP 30 Feritscope. A total of 16 readings were taken on each specimen, and the average values were calculated. Figure 2 shows the front view of the specimens where ferrite content

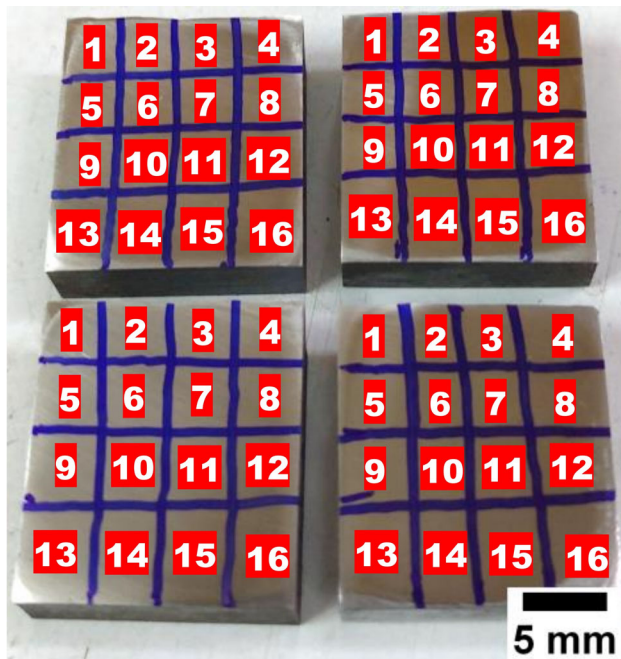


Figure 2 Front view of the specimens showing the locations where ferrite content readings were taken.

readings were taken. For phase identification, the specimens were subjected to X-ray diffraction (XRD) analysis. The parameters used to obtain XRD spectra were: 2θ scan range 20° – 100° , step size: 0.02° , and time per step equal to 1.5 s.

Corrosion testing

The corrosion tests were conducted on specimens polished up to 1000-grit SiC abrasive papers in neutral-chloride (3.5% NaCl) as well as acidic-chloride (0.5 M H_2SO_4 + 0.5 M NaCl) solutions at room temperature using a Potentiostat. The testing system was a conventional three-electrode setup comprising of saturated calomel electrode (SCE) as the reference, graphite as the counter, and specimen surface as the working electrode.

The specimens were subjected to linear polarization resistance (LPR) measurements, Tafel scan (potentiodynamic polarization), electrochemical impedance spectroscopy (EIS), potentiodynamic anodic polarization (PAP), and cyclic potentiodynamic polarization (CPP) tests. Before performing any test, the specimens were immersed for 3600 s in the test solution to establish a quasi-stable state of the open-circuit potential (E_{oc}). The LPR tests were conducted by polarizing the specimens ± 15 mV about

their E_{oc} at a very slow scan rate of 0.125 mV/s. The analysis of the output LPR test curves gave the values of polarization resistance (R_p), which is a parameter inversely related to the uniform/general corrosion rate. For a relatively more accurate study on the general corrosion behavior, the Tafel scan (potentiodynamic polarization) was performed. The polarization of the specimens, in this case, was carried out ± 250 mV about the E_{oc} at a very slow scan rate of 0.125 mV/s. To study the corrosion behavior based on the nondestructive AC-based technique, EIS tests were performed in the potentiostatic mode by applying a 10 mV_{rms} sinusoidal perturbation signal. The frequency range was 1,000,000 to 0.01 Hz, and the points per decade were 10. The EIS results were interpreted by fitting the experimentally obtained impedance spectra to a suitable equivalent electrical circuit (EEC) model to extract various electrochemical performance parameters quantitatively. For studying pitting corrosion behavior, PAP tests were conducted from a starting potential of -0.1 V vs. E_{oc} up to an apex potential of 1.5 V with respect to E_{oc} at a scan rate of 1 mV/s. It involved potentiodynamic scanning only in one direction towards anodic values relative to the E_{oc} . The specimens were subjected to CPP tests also involving potentiodynamic scanning in a cyclic manner to get insights into repassivation characteristics subsequent to pitting. From the CPP technique, the tendency of specimens to pit formation and pit growth was determined. These tests were performed with the forward scan commencing at E_{oc} and going up to an apex potential of 1.5 V relative to E_{oc} , with the apex current density value set at 10 mA/cm². The scan was reversed when either the apex current or voltage value was reached. The reverse scan was stopped at 0 V vs. E_{oc} . The scan rate used was 1 mV/s. For reproducibility of the results, corrosion experiments (Tafel scan, PAP, and CPP tests) were repeated due to the destructive nature of these techniques, since the extent of polarization involved is sufficient to cause a permanent change in the surface condition of the specimen.

Results and discussion

Microstructural characterization

SEM images of DSS 2205 base metal microstructure at different magnifications are presented in Fig. 3a–c.

The microstructure of the base metal was comprised of two phases, viz. austenite (γ) and ferrite (α) present in comparable proportions. The γ was present in the form of bands in the continuous α matrix [20]. The α/γ interfacial, as well as α matrix regions, were free from any secondary phases.

Before discussing the microstructure of the weld metal which was formed after the base metal was EB-welded, it is important to understand the microstructural evolution process in DSS welds. Figure 4a–d schematically illustrates how the microstructure forms in weld metal during solidification under an adequate cooling rate. For a given weld metal composition, an adequate cooling rate is the one that allows for sufficient ferrite-to-austenite transformation and it is fast enough to prevent the precipitation of intermetallics such as σ and χ . During solidification, a completely ferritic structure is initially formed from the liquid by primary

crystallization (Fig. 4a). On further cooling, the solid-state transformation of ferrite to austenite occurs below the solidus temperature. Depending on the cooling rate and chemical composition of weld metal, austenite can form in different morphologies [12, 21]. Due to the higher free energy at prior α/α grain boundaries, austenite forms in the form of grain boundary allotriomorphs outlining these ferrite grain boundaries as shown in Fig. 4b. This first type of austenite is called grain boundary austenite (GBA). The GBA formation occurs in a wide temperature range of 1350 °C to 800 °C [8, 22]. With the further decrease in temperature, the proportion of GBA increases as a consequence of which the available nucleation sites at the α/α boundaries decrease and new nuclei begin to form at α/γ interfaces [8].

As shown in Fig. 4c, the new austenite nuclei grow from GBA towards inside the ferrite grains as side-plates Widmanstätten austenite (WA) [22]. The

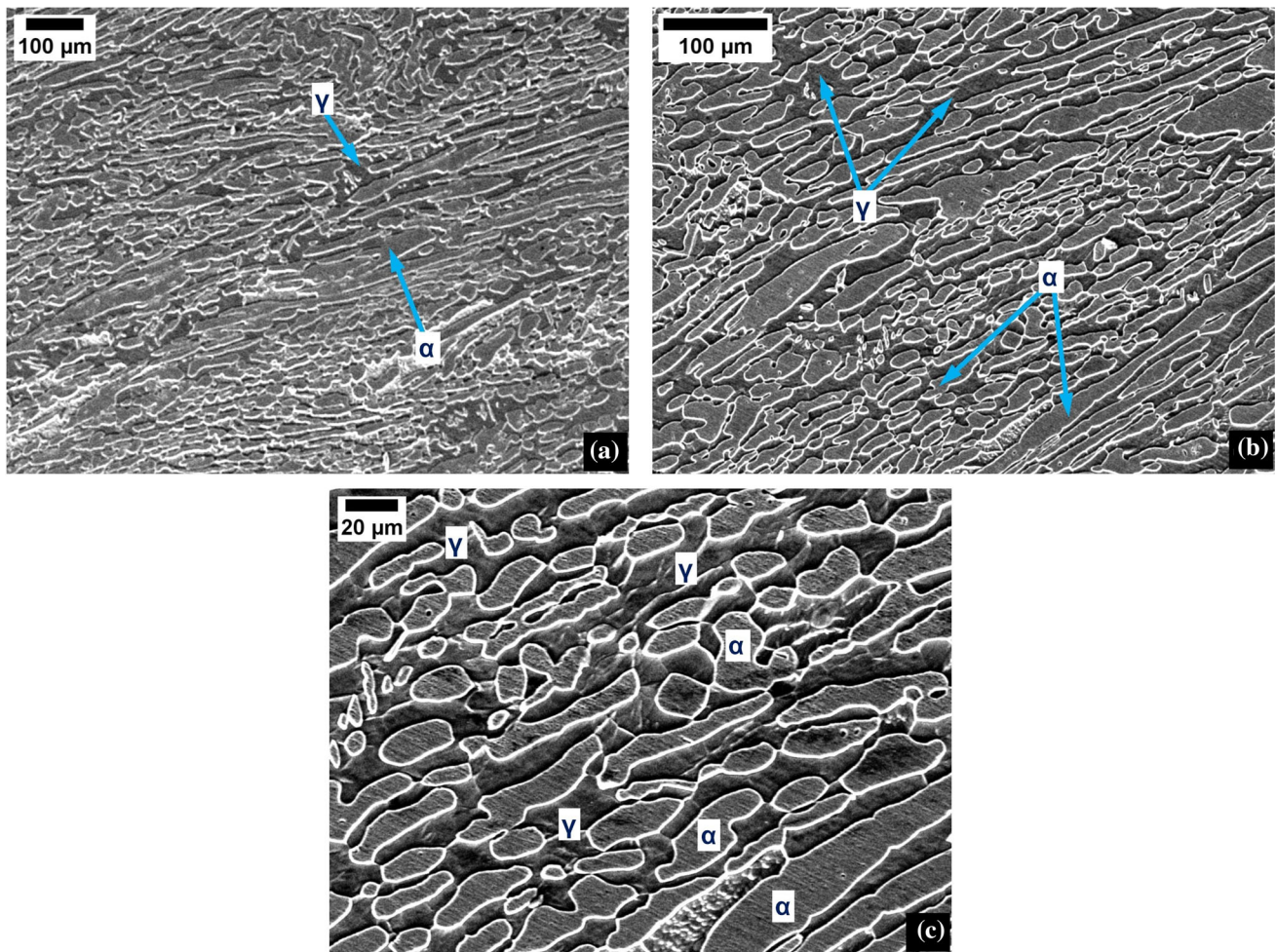


Figure 3 SEM images of the base metal in the as-received condition at different magnifications **a** $\times 110$, **b** $\times 200$, and **c** $\times 500$.

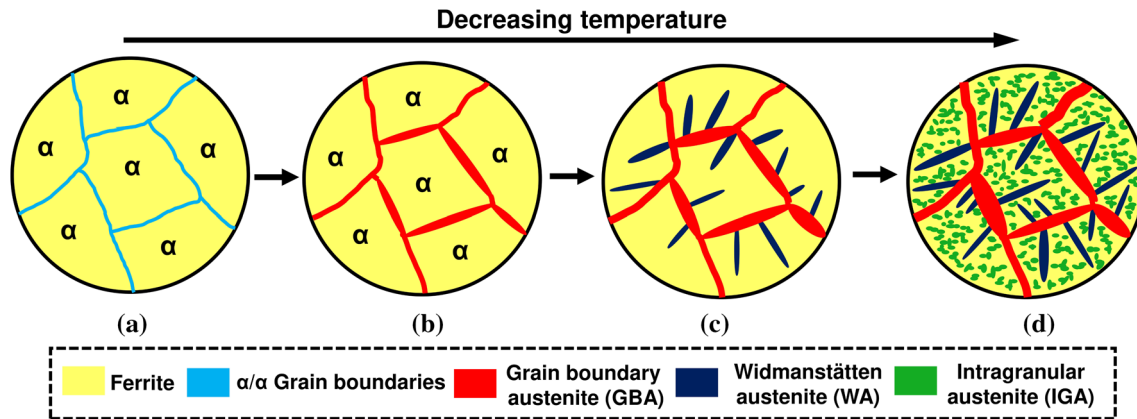


Figure 4 Schematic illustration of microstructural evolution during solidification in DSS weld metal under an adequate cooling rate.

formation of WA occurs in the temperature range of 650 °C to 800 °C [8]. Lastly, austenite nucleates in the form of intragranular austenite (IGA) particles within the ferrite grains as shown in Fig. 4d. The formation of GBA and WA requires a smaller driving force, and they form at higher temperatures with little undercooling, whereas IGA forms at relatively lower temperatures. The IGA is finer and equiaxed compared to GBA and WA because of the significantly slower lattice diffusion within the ferrite than in the grain boundary [22]. During EB welding, the molten weld pool undergoes rapid cooling; therefore, the microstructure of the weld metal markedly deviates from a balanced two-phase α/γ ratio.

While examining the weld metal (surface subjected to a single thermal cycle during EBW) in the present study, demarcation could be made between weld top and bottom regions based on noticeable differences in their microstructure. SEM images of the weld metal near top and bottom regions are shown at different magnifications in Fig. 5a–f. The region near weld top contained coarse polygonal ferrite grains with the presence of GBA, WA, and IGA in a continuous ferrite matrix (Fig. 5a, b). Although WA formation was observed in the weld metal, it was present to a much lesser extent, whereas GBA and IGA were relatively more dominant (Fig. 5c). In comparison with weld top, the ferrite grains towards weld bottom region were noticeably smaller (Fig. 5d, e). Comparing the high-magnification SEM images (Fig. 5c and f), it was clear that the overall volume fraction of austenite was relatively more near weld top region compared to weld bottom region. The GBA was thicker, WA sideplates were longer, and the IGA volume fraction was noticeably more towards weld top region. There were

two key observations from the microstructural examination of the weld metal. The first one was that the overall austenite proportion was relatively less compared to ferrite in the weld metal. Rapid cooling rates associated with the thermal cycle of EBW, and loss of nitrogen during autogenous welding are the two reported reasons for relatively less austenite formation in DSS EB welds [11, 12, 23]. The second one was the microstructural differences between weld top and bottom regions. The presence of relatively more austenite near weld top suggested that this region experienced a relatively slower cooling rate than the region near bottom of the weld. The differences in cooling rate near weld top and bottom regions could be attributed to the tapered geometry of the weld bead (Fig. 1b). Owing to the larger width (hence larger weld volume) near top region, cooling rates were expectedly slower compared to bottom or root region where weld width (hence weld volume) was smaller. It has been reported in the case of EB DSS welds that relatively slow cooling rates near upper region favor the ferrite-to-austenite transformation, and therefore it contained a relatively higher amount of austenite compared to weld bottom/root region [13]. Similar to the present results, Xia et al. [24] observed microstructural variations from top to bottom part in thick-Sect. 316L austenitic SS electron beam welds, and it was reported that bottom part of the weld experienced a relatively faster cooling rate during weld solidification compared to top.

Furthermore, as shown in Fig. 5d, e, a few corrosion pits were observed near bottom region of the weld metal. These small pits have been reported to be associated with the presence of Cr-nitride precipitates in rapidly cooled DSS welds [10]. Due to

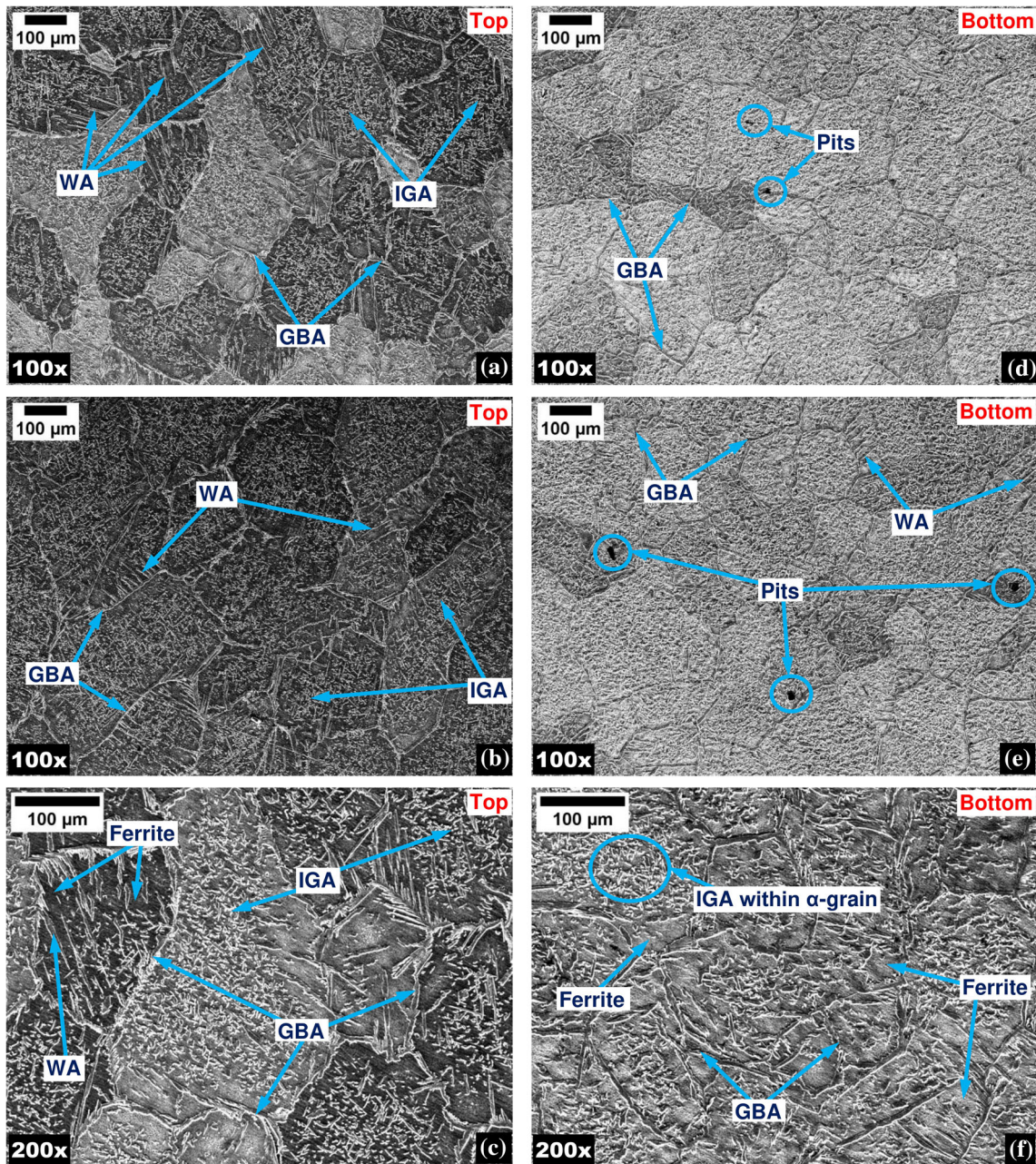


Figure 5 SEM images of the weld metal at different magnifications near **a–c** top region and **d–f** bottom region.

relatively higher cooling rates, nitrides have a greater tendency to precipitate near bottom region compared to top surface in DSS welds [12, 25].

The microstructure of the base metal after aging is depicted in SEM images taken at different magnifications (Fig. 6a, b). In contrast to the base metal in the as-received condition, the α/γ interfacial regions, as well as α -matrix in the aged base metal, contained a significant amount of secondary precipitation. There were clear signs that ferrite underwent

decomposition after thermal aging treatment. The precipitation that occurred was characterized by heterogenous nucleation and growth. As shown in Fig. 6a, some regions comprising α/γ boundaries and ferrite grains showed much lesser signs of precipitation, whereas some regions were affected to a much higher extent.

Furthermore, it was noted that austenite was largely unaffected due to aging, and observation at a higher magnification revealed no noticeably

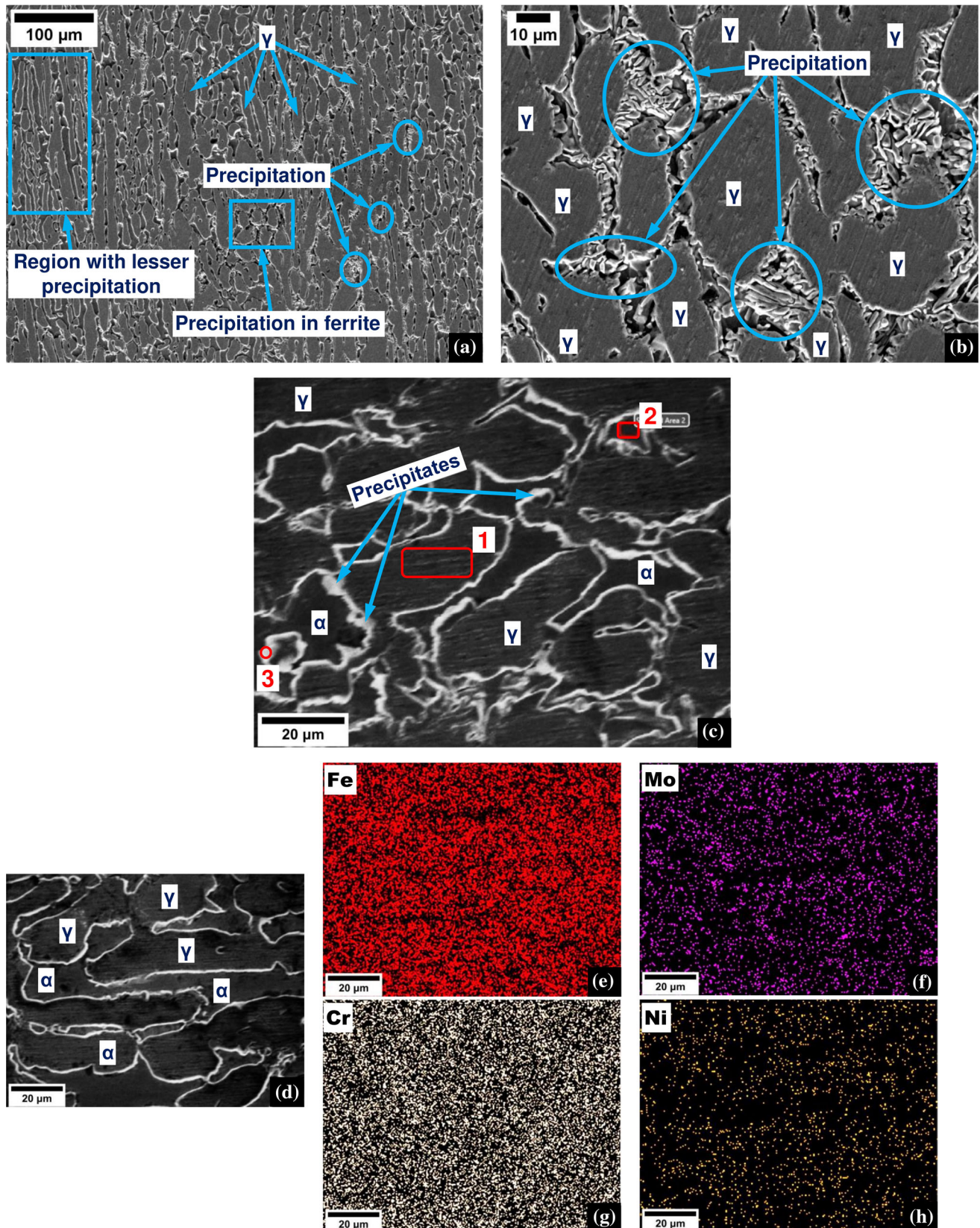


Figure 6 a, b SEM images of the aged base metal at $\times 200$ and $\times 850$ magnification, respectively, c locations where the composition was analyzed using EDS, d SEM image on which EDS mapping was done, and e–h EDS mapping results.

significant changes in surface morphology of austenite (Fig. 6b) compared to ferrite. Similar microstructural observations of secondary phase formation at grain boundaries and growth into ferrite phase for DSS 2205 subjected to aging at 850 °C have been reported [26].

In the case of as-received DSS base metal, partitioning of alloying elements exists between austenite and ferrite. The ferrite has a higher content of ferrite stabilizing elements such as Cr and Mo, and a lower content of austenite stabilizing elements such as Ni in comparison with austenite [20, 23, 25, 27]. In a study on EB-welded 2205 DSS, the average composition (wt%) determined by EDS microanalysis for the base metal ferrite was reported to be 22.98% Cr, 4.06% Ni, 4.52% Mo, whereas for austenite it was 21.59% Cr, 5.58% Ni, 2.63% Mo [27]. In the present work, EDS studies were carried out to gain insights into aging-induced compositional variations.

SEM image of the aged base metal is shown in Fig. 6c, along with locations marked where the composition was analyzed using EDS, and the results are presented in Table 4. The composition of austenite (location 1) was slightly low in Cr (20.8 wt%) and Mo (1.5 wt%), slightly rich in Ni (5.8 wt%), and significantly high in N (5.5 wt%) compared to nominal alloy composition. The ferrite (location 2) on the other hand showed significant enrichment in Cr (28.1 wt%) without any proportionate rise in Mo (0.7 wt%). Location 3 targeted on a precipitate (Fig. 6c) was rich in Cr (24 wt%) as well as Mo (8.5 wt%) and contained lower Ni (2.4 wt%) compared to austenite and ferrite. The effect of aging was reflected in EDS results when compared with the compositional aspects of as-received base metal [20, 27]. To

characterize the segregation of elements, EDS area mapping was employed (Fig. 6d). The mapping results of different elements are shown in Fig. 6e–h. The various regions noticeably depleted in Fe, Mo, Cr, and Ni could be observed in the aged base metal.

Figure 7a and b shows the microstructure of the aged weld metal near top and bottom regions, respectively. The effect of aging treatment on the microstructure of the weld metal was perceptible when compared to its as-welded counterpart. It was again noteworthy that ferrite grains were smaller near weld bottom region compared to top region.

EDS results for higher-magnification image (Fig. 7c) are presented in Table 4. Firstly, it is important to discuss the compositional aspects of microstructural phases for the as-welded DSS EB weld metal. As discussed previously, the as-received base metal exhibits differences in the composition of austenite and ferrite. When subjected to EB welding, the diffusion of alloying elements into ferrite and austenite gets suppressed due to the rapid cooling of the molten weld pool [23]. Due to the high cooling rates involved in the weld thermal cycle, the experimental partitioning ratios of the substitutional elements in the DSS EB weld zone have been reported to be close to 1, and austenite and ferrite had almost the same chemical composition [12, 27]. In the present study, the composition was analyzed for the aged weld metal. The concentration of different elements such as Cr, Ni, and Mo in austenite grains (locations 1, 2, and 3) of different sizes was largely close to each other (Table 4). The pronounced effect of aging-induced precipitation was revealed from the composition of location 4 taken within the matrix region. A significantly high Cr concentration (29.3 wt%) was observed. Conversely, this location was significantly deficient in Mo. Unlike austenite, the matrix region had much lower Ni (1.9 wt%) and N (0.6 wt%) concentrations. EDS area mapping was done on the aged weld metal (Fig. 7d), and the maps of various elements are presented in Fig. 7e–h. Similar to the aged base metal, the various regions depleted in Fe, Mo, Cr, and Ni could be observed in the weld metal. It was noteworthy that for the base metal, the depleted regions were noticeably wider and continuous compared to the weld metal. Overall, the EDS results evidenced the existence of significant compositional heterogeneity in the microstructure of both the weld metal and base metal in the aged condition. Such compositional heterogeneity in the microstructure

Table 4 EDS results for the base metal and weld metal specimens in the aged condition

	Region	Cr (wt%)	Ni (wt%)	Mo (wt%)	N (wt%)	Fe (wt%)
Figure 6c	1	20.8	5.8	1.5	5.5	66.4
	2	28.1	4.7	0.7	0.4	66.1
	3	24.0	2.4	8.5	5.7	59.4
Figure 7c	1	22.4	6.1	1.8	2.5	67.2
	2	20.6	8.1	1.8	1.6	67.9
	3	21.0	6.3	2.1	3.3	67.3
	4	29.3	1.9	0.8	0.6	67.4

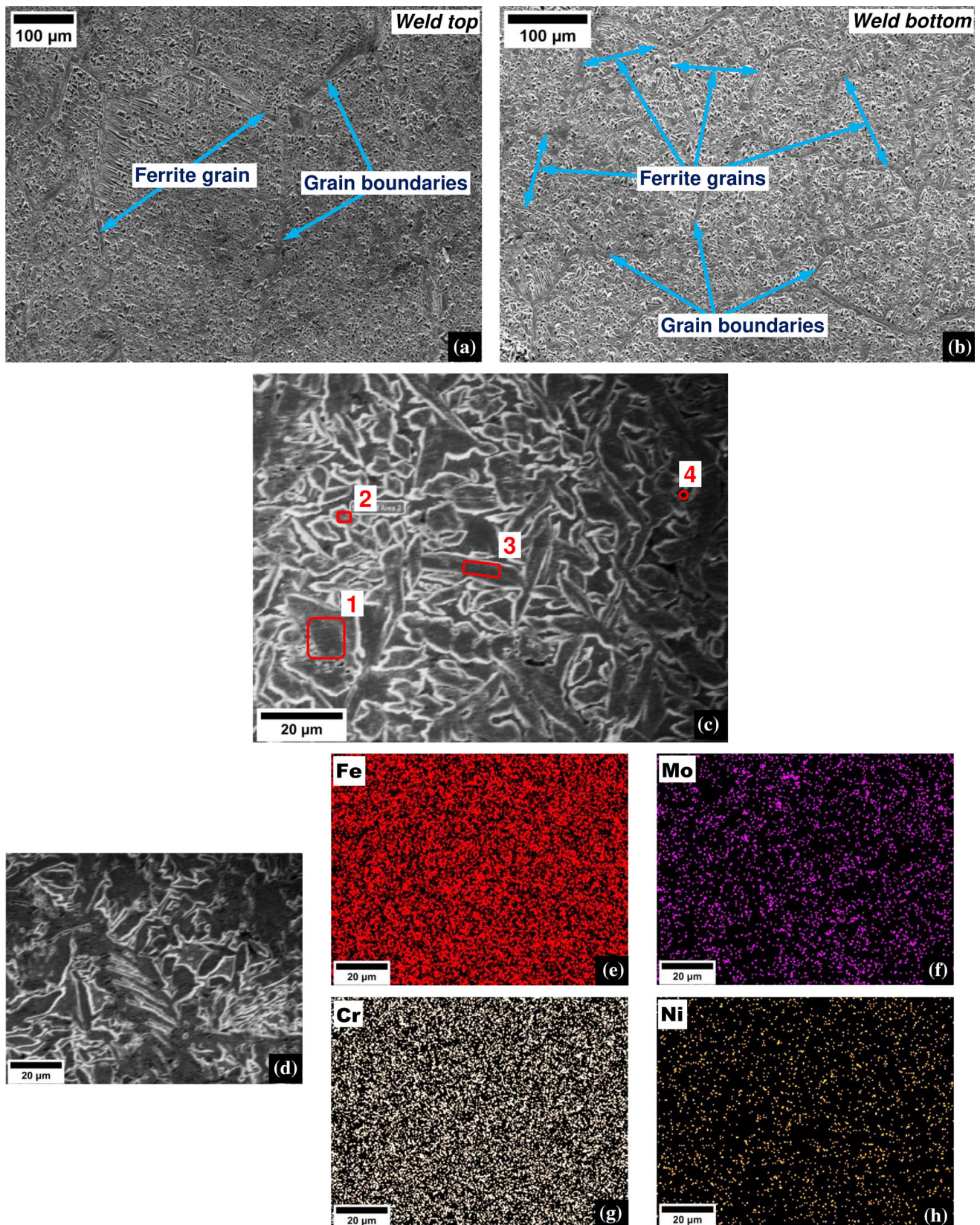


Figure 7 a, b SEM images of the aged weld metal taken near weld top and bottom region, respectively, c locations where the composition was analyzed using EDS, d SEM image on which EDS mapping was done, and e–h EDS mapping results.

could be attributed to the formation of secondary phases due to aging treatment.

Ferrite content and XRD studies

To study the role of EB welding as well as aging in causing phase transformations, ferrite content measurements were done using Feritscope. These measurements were based on the magnetic permeability of steel and were nondestructive. In DSSs, ferrite is a ferromagnetic phase unlike other phases such as austenite, sigma, and Cr-nitrides. Figure 8 shows the average ferrite percentage for different specimens. The base metal showed an average ferrite content of $\sim 50.15\%$, whereas the weld metal showed a higher ferrite content of $\sim 71.39\%$. The phase imbalance ($\alpha > \gamma$) in the weld metal was mainly attributable to rapid cooling involved in EB welding which suppressed the diffusion-controlled $\alpha \rightarrow \gamma$ transformation. After isothermal aging, there was a decrease in ferrite content of both the base metal and weld metal with values amounting to $\sim 25.06\%$ and 36.03% , respectively. The extent of ferrite content reduction was almost the same for both specimens. The decrease in ferrite content was an indication of its decomposition to secondary phases which appear in a stable state under such conditions [28].

To ascertain the type of secondary phases that were formed due to aging, the specimens were subjected to XRD analysis. XRD patterns for the weld metal in the as-welded and aged conditions are shown in Fig. 9a. For the as-welded condition (WM0), the weld metal showed the presence of primary microstructural

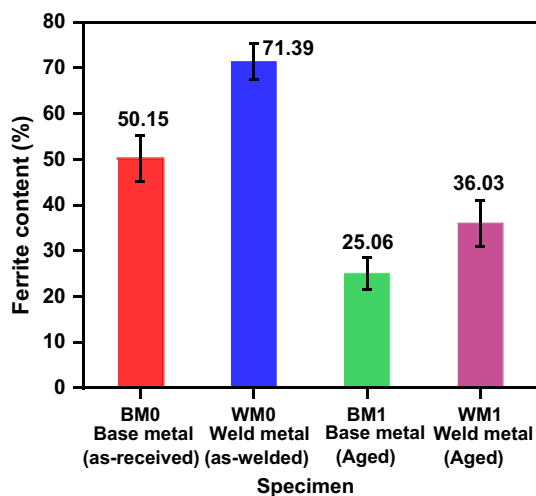


Figure 8 Average ferrite percentage for different specimens.

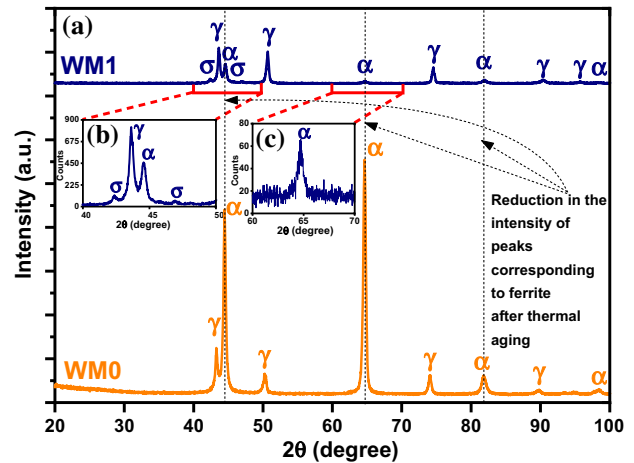


Figure 9 XRD patterns for the specimens WM0 (weld metal in the as-welded condition) and WM1 (weld metal in the aged condition).

phases, viz. austenite and ferrite. The intensity of peaks corresponding to ferrite was much higher compared to austenite, thus indicating that microstructural phase imbalance existed in the weld metal, i.e., ferrite was present in a higher amount compared to austenite. The effect of aging on microstructural phases of the weld metal could be observed from the XRD pattern of the aged weld metal which presented noticeable differences compared to the XRD pattern of WM0. In this case, peaks corresponding to σ -phase were detected between 40° and 50° (Fig. 9b). Similar results evidencing the formation of σ -phase in DSS aged at 850°C have been reported [14, 15, 18]. Another important observation was of reduction in the intensity of ferrite peaks along with a slight increase in the intensity of austenite peaks which has been reported to be due to the formation of secondary austenite (γ_2) [14]. A significant reduction in ferrite (Fig. 9c) indicated that a major portion of it was subject to decomposition and transformed into σ -phase. It has been reported that σ -phase has a tetragonal structure and is a product of the transformation of ferrite to σ -phase, and it precipitates at high Cr-concentrated regions [29]. Ferrite is a favorable site for precipitation of σ -phase.

The precipitation rate of σ -phase from ferrite is relatively higher, and its preferential growth into ferrite is mainly the result of higher Cr and Mo concentrations in ferrite [29]. At 850°C , σ -phase can form in DSS by three mechanisms, viz. nucleation and growth from original ferrite, eutectoid decomposition of ferrite involving the formation of

secondary austenite ($\alpha \rightarrow \sigma + \gamma_2$), and growth from austenite after total consumption of original ferrite [15]. Overall, it could be deduced that σ -phase precipitation due to aging was strongly related to the consumption of ferrite phase. To study the implications of such microstructural transformations on corrosion properties, the specimens were subjected to corrosion tests in two different solutions.

Corrosion studies in 3.5% NaCl solution

The LPR test curves for the specimens are presented in Fig. 10a. The parameter obtained from this test was the polarization resistance (R_p), which is an indicator of resistance to general/uniform corrosion and is inversely related to the uniform corrosion rate. The base metal in the as-received condition showed the best resistance to general corrosion as indicated by its highest R_p . There was a marked drop (> 50%) in its R_p after EB welding, which indicated that the weld metal had lower general corrosion resistance than the

base metal [12]. The higher corrosion resistance of the base metal could be attributed to its balanced microstructure devoid of any secondary phases and comprising ferrite and austenite in comparable amounts, unlike the weld metal. The aged base metal showed a loss in corrosion resistance (due to a decrease in R_p) compared to the as-received condition. On the contrary, it was noted that such type of corrosion resistance degradation did not occur for the weld metal after aging. In fact, in this case, the average R_p was higher compared to the as-welded condition, although both the weld metal and base metal were subjected to the same aging treatment which promoted precipitation in the microstructure. It was, therefore, important to confirm the corrosion resistance order with other techniques also.

The specimens were further subjected to potentiodynamic polarization test, and the results are presented in Fig. 10b. The value of corrosion current density (i_{corr}) was determined by locating the intersection point of cathodic and anodic slope lines, i.e.,

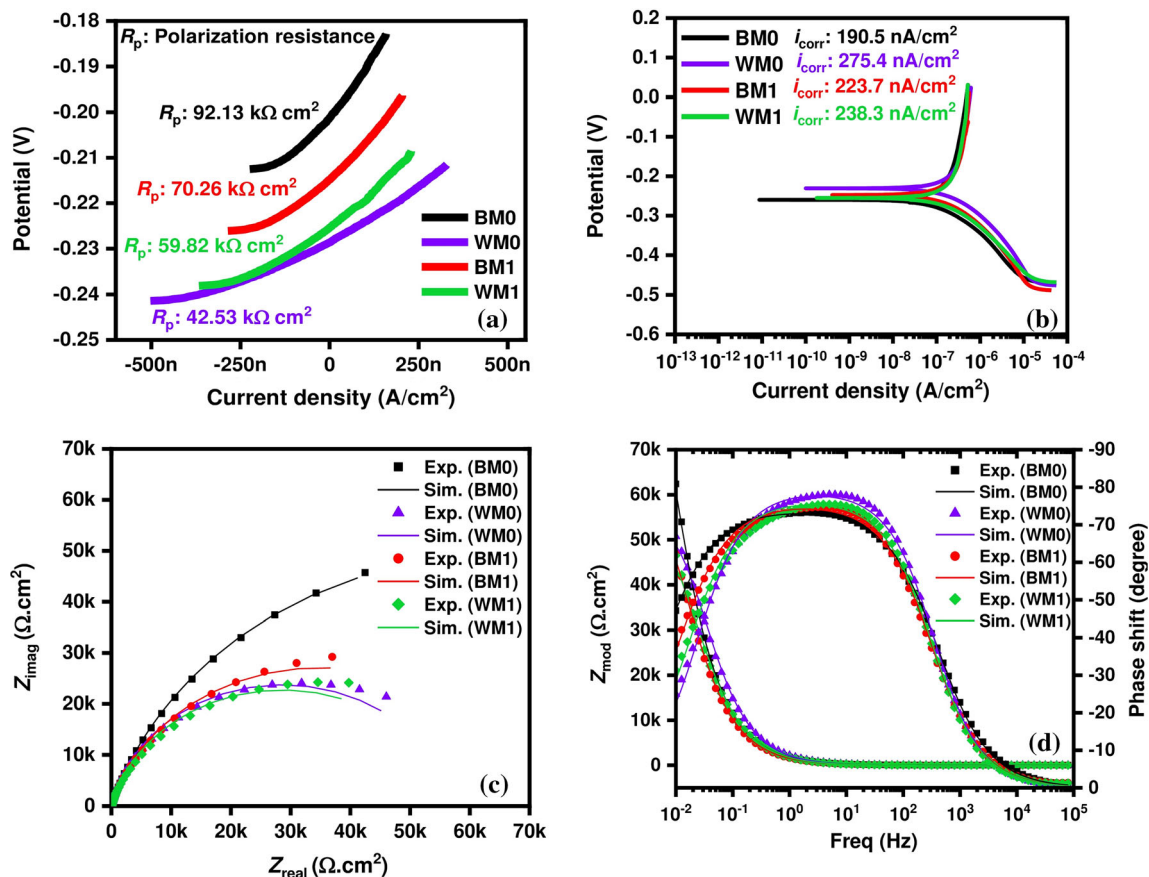


Figure 10 a LPR test curves, b Tafel scan (potentiodynamic polarization test) curves, c Nyquist plots, and d Bode plots for the specimens tested in 3.5% NaCl solution.

extrapolation of the linear part of the polarization curves (anodic and cathodic) to corrosion potential (E_{corr}). The i_{corr} is essentially an indicator of general corrosion resistance and is directly proportional to the general corrosion rate [30]. High values of i_{corr} imply higher susceptibility towards electrochemical dissolution in a corrosive environment. The base metal showed the lowest i_{corr} ($\sim 190.5 \text{ nA/cm}^2$) and hence the best corrosion resistance. The weld metal showed higher i_{corr} ($\sim 275.4 \text{ nA/cm}^2$), indicating that its corrosion resistance was lower than the base metal. There was an increase in i_{corr} for the base metal after aging ($i_{\text{corr}} \sim 223.7 \text{ nA/cm}^2$) which implied a loss in corrosion resistance occurred after aging. The passive film formation is one of the key characteristics of stainless steels due to which they exhibit excellent corrosion resistance. The compositional heterogeneity (due to welding or aging-induced precipitation), however, adversely affects the stability of the passive film and thus their corrosion resistance [31]. The loss in corrosion resistance of the base metal could be attributed to compositional heterogeneity caused due to aging-induced precipitation as indicated by SEM/EDS results. On the contrary, the weld metal showed a lower i_{corr} after aging compared to its as-welded counterpart. Both LPR and the potentiodynamic test showed a similar corrosion resistance trend for these specimens. The corrosion behavior of the aged weld metal was unexpected, as, despite its microstructure being characterized by compositional heterogeneity and the presence of σ -phase, its corrosion resistance did not undergo an expected decrease, unlike the base metal.

The specimens were further subjected to EIS measurements to substantiate the results obtained with the DC-based polarization techniques. The results are presented as Nyquist (Fig. 10c) and Bode plots (Fig. 10d). The Nyquist plots showed unfinished semicircular arcs. Such a type of profile is indicative of a mechanism of charge transfer on an inhomogeneous surface [16]. The general profile of the spectra was similar for all the specimens with noticeable differences in the size of unfinished semi-circular arcs. A larger diameter of the arc is indicative of higher impedance or higher hindrance in charge transfer, and therefore, higher corrosion resistance. The arc size for the base metal was larger than the weld metal, indicative of higher stability and protectiveness of its passive film, and therefore higher resistance to electrochemical dissolution than the

weld metal. From the Bode magnitude plots, a higher impedance value was noted for the base metal compared to weld metal (Fig. 10d). The phase shift for the base metal in the low-frequency region was higher than the weld metal, but its peak value was lower than the weld metal. After aging, there was a notable drop in impedance of the base metal as observed from Nyquist and Bode magnitude plots. On the other hand, the spectra were relatively less distinguishable for the weld metal. The quantitative analysis of EIS data was done using fitting to an equivalent electrical circuit (EEC) model ($R_s(-\text{CPE} || R_{\text{ct}})$) representing a one-time constant [32]. In the EEC model, R_s represents the solution resistance, CPE represents the constant phase element, and R_{ct} is an indicator of oxide film stability and represents the charge transfer resistance through the passive film and across the interface with the electrolyte and is inversely related to the corrosion rate of the system. The impedance function of a CPE is given by the following equation:

$$Z_{\text{CPE}} = Q^{-1}(j\omega)^{-n}$$

where parameter Q is the CPE magnitude, n is the CPE exponent, ω is the angular frequency, and $j = i$. The exponent n can be employed as a gauge of heterogeneity of the surface [33]. Its value equal to $-1, 0, 1$ corresponds to an inductor, a resistor, and a capacitor, respectively, and represents the capacitance dispersion [16]. The results obtained after fitting experimental spectra to the EEC model are given in Table 5. The function χ^2 represents the difference between the experimentally obtained and simulated spectra. The values of the order of 10^{-3} were suggestive of a good fit, thus justifying the employed EEC model. In Fig. 10c, d, the experimental and simulated spectra are represented by symbols and solid lines, respectively, and depict close resemblance. The value of R_s was nearly the same for all the specimens and was very low compared to R_{ct} . The resistance of the passive layer formed on the base metal was the highest, and it exhibited the best corrosion resistance. The weld metal showed a significantly lower R_{ct} , which meant that the corrosion resistance of DSS decreased after EB welding. Furthermore, there was a significant drop in R_{ct} of the base metal after aging, while the weld metal after aging did not exhibit such a loss in corrosion resistance, as its R_{ct} was comparable to its as-welded

Table 5 Parameters obtained after fitting the experimental impedance spectra to the equivalent electrical circuit model for different specimens tested in 3.5% NaCl solution

Specimen	R_s ($\Omega \text{ cm}^2$)	CPE, Q ($\Omega^{-1} \text{ cm}^{-2} \text{ s}^n$)	R_{ct} ($\Omega \text{ cm}^2$)	n	Goodness of Fit (χ^2)
BM0	$12.78 \pm 65.02\text{e-}3$	$122.4\text{e-}6 \pm 698.3\text{e-}9$	$130.1\text{e}3 \pm 4.370\text{e}3$	$822.3\text{e-}3 \pm 1.363\text{e-}3$	$16.49\text{e-}3$
WM0	$12.46 \pm 61.34\text{e-}3$	$91.11\text{e-}6 \pm 574.6\text{e-}9$	$57.32\text{e}3 \pm 827.6$	$880.8\text{e-}3 \pm 1.455\text{e-}3$	$10.20\text{e-}3$
BM1	$12.19 \pm 59.59\text{e-}3$	$137.7\text{e-}6 \pm 815.8\text{e-}9$	$69.84\text{e}3 \pm 1.543\text{e}3$	$840.5\text{e-}3 \pm 1.429\text{e-}3$	$2.433\text{e-}3$
WM1	$12.53 \pm 61.10\text{e-}3$	$119.3\text{e-}6 \pm 731.9\text{e-}9$	$57.23\text{e}3 \pm 1.004\text{e}3$	$854.8\text{e-}3 \pm 1.452\text{e-}3$	$2.014\text{e-}3$

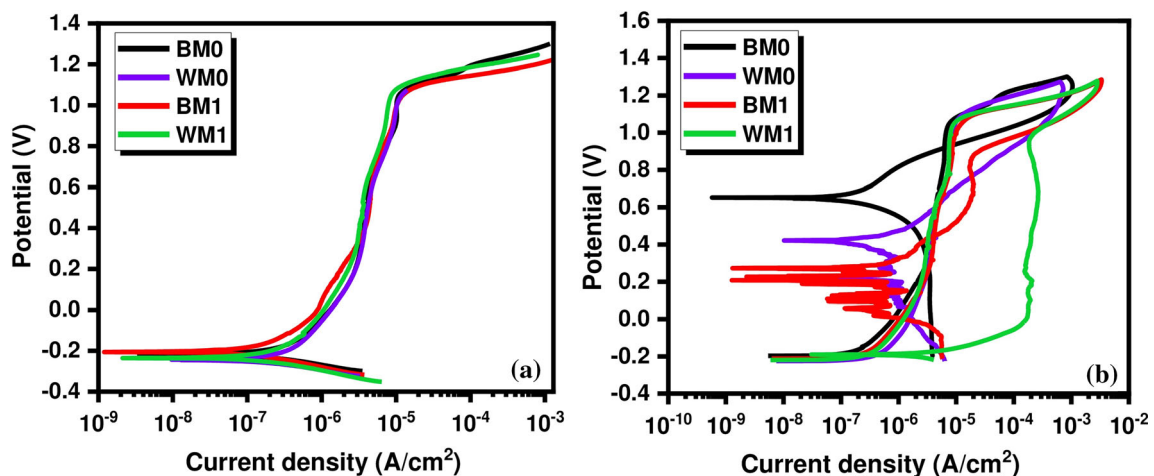
counterpart. It has been reported that Q is inversely related to passive layer thickness [5, 33].

The variation in parameter Q indicated that there were differences in passive layer thickness for these specimens but with no particular order with respect to the R_{ct} trend. It could be seen that the value of n was less than 1 for all the specimens, which has been reported to be indicative of a frequency-dependent capacitor that shows the characteristic behavior of an oxide film [34]. The value of n was the highest for the weld metal while it was the lowest for the base metal. Based on the EIS results, it could be deduced that the oxide film resistance of the base metal underwent degradation after EB welding, as a result of which the weld metal showed relatively weaker general corrosion resistance compared to the base metal [35]. While there was a marked loss in the passive film stability of the base metal after aging, the passive film on the weld metal did not undergo such degradation despite the presence of intermetallic σ -phase in the aged weld metal. Overall, the results from LPR, Tafel scan, and EIS tests indicated that thermal aging influenced the corrosion behavior of the weld metal and base metal differently, as these specimens in the aged condition did not show a consistent trend with

respect to their as-welded/unaged counterpart. It was, therefore, important to study their localized (pitting) corrosion behavior as well.

The specimens were subjected to PAP scan to evaluate their pitting behavior, and their representative curves are presented in Fig. 11a. Pitting potential (E_{pit}) was taken as the indicator of resistance to pitting corrosion [36] and is represented by the potential after which anodic current density rapidly increases.

All the specimens exhibited passive behavior up to potential values exceeding 1000 mV. E_{pit} was more or less the same and was in a close range for all the specimens as the curves were almost identical. Furthermore, corrosion potential (E_{corr}), and thus ($E_{pit} - E_{corr}$) values were also in a close range for these specimens. The rapid rise in current density during anodic polarization in the passive range, apart from passive film breakdown and pit formation, could also be due to the evolution of oxygen by the decomposition of water [37]. If the increase in current density is due to the decomposition of water and oxidation evolution, the region is termed as transpassive region [37]. The confirmation concerning the same is obtained by visual examination of the specimen surface after the test. The present results indicated

**Figure 11** a PAP scan curves and b CPP scan curves for the specimens tested in 3.5% NaCl solution.

that microstructural phase imbalance or σ -phase precipitation did not significantly affect the resistance to pitting corrosion initiation. Different results exist in the literature concerning the relationship between σ -phase and pitting corrosion resistance for DSSs. Many studies have reported the deleterious effect of σ -phase on pitting resistance, as it results in the creation of regions depleted in key elements such as Cr and Mo responsible for imparting resistance against pitting [2, 4, 6, 13, 14]. In a study on pitting corrosion behavior of isothermally aged DSS, it was reported that loss in E_{pit} was caused by the precipitation of σ -phase, and E_{pit} decreased with an increase in aging time [29]. He et al. [38] reported that Cr is the main element in the passive film of DSS, and its depletion in the vicinity of σ -phase is the major reason for causing deterioration in pitting corrosion resistance. On the contrary, Yongqiang et al. [16] reported that pitting of DSS due to σ -phase precipitation is mainly due to the difference in Cr content between σ -phase and Cr-depleted zone, and not only to the Cr-depleted zone itself. They observed that more sigma phase formation did not always result in lowering the pitting resistance of DSS, and higher pitting resistance could be obtained despite the presence of a large amount of sigma phase. In the present study, the important point to note was that these specimens were characterized by marked microstructural differences be in terms of phase imbalance caused by welding or σ -phase precipitation due to aging treatment. They could not be ranked based on their pitting corrosion behavior using the PAP test. Although the effect of such microstructural differences was reflected in the results of corrosion studies carried out using LPR, potentiodynamic polarization, and EIS tests, the anodic polarization process was not affected significantly. As microstructure plays an influential role in the corrosion characteristics of DSSs, it was

important to accurately rank these specimens based on their pitting behavior, since they were characterized by distinct microstructural features. Their localized corrosion susceptibility was, therefore, further evaluated using the CPP technique.

Representative CPP scan curves for the specimens are presented in Fig. 11b. The values of corrosion potential (E_{corr}), pitting/breakdown potential (E_{pit}), and repassivation/protection potential (E_{rp}) are given in Table 6. E_{pit} corresponds to the potential at which the passivation is no longer dominant, and passive film undergoes breakdown and stable pitting occurs [39, 40]. E_{rp} corresponds to the potential at which the reverse scan curve intersects with the forward scan curve. It is the potential at which the growth of initiated corrosion pits stops, or in other words, repassivation occurs [36, 37]. Materials exhibiting nobler values of both E_{pit} and E_{rp} are considered to be more resistant to pitting [41]. All the specimens exhibited a spontaneous passivity up to a very high potential exceeding 1000 mV, which signified a high resistance to the initiation of pitting corrosion. The E_{pit} values were in the range of ~ 1023–1050 mV. Furthermore, the values of E_{corr} were also in a close range (Table 6). Both E_{pit} and ($E_{pit} - E_{corr}$) are reported to be indicators of pitting corrosion resistance [36].

Two factors related to the microstructure, viz. phase imbalance and precipitation of σ -phase, did not affect pitting resistance significantly considering the extent of change in ferrite content observed, which was consistent with the PAP test results. There were, however, notable differences in E_{rp} among these specimens. The base metal during the reverse scan repassivated at a significantly high potential. The weld metal also displayed a similar behavior but repassivation, in this case, was much delayed compared to the base metal. The difference between

Table 6 Cyclic potentiodynamic polarization testing results

Test solution	Specimen	E_{corr} (mV)	E_{pit} (mV)	E_{rp} (mV)	$E_{pit} - E_{corr}$ (mV)	$E_{pit} - E_{rp}$ (mV)
3.5% NaCl	BM0	- 199.5	1050	922.7	1249.5	127.3
	WM0	- 224.27	1047	608.5	1271.27	438.5
	BM1	- 211	1023	447.5	1234	575.5
	WM1	- 220.7	1033	- 187.8	1253.7	1220.8
0.5 M H ₂ SO ₄ + 0.5 M NaCl	BM0	- 76.85	875.7	942	952.55	-
	WM0	- 112.4	870.2	127.1	982.6	743.1
	BM1	- 67.35	867.4	-	934.75	-
	WM1	- 130.5	865.5	16.57	996	848.93

$E_{\text{pit}} - E_{\text{rp}}$ indicates pitting corrosion susceptibility [7, 37]. The larger the difference between E_{pit} and E_{rp} , the poorer will be the resistance to pit growth, as the pits initiated after E_{pit} is reached continue to grow until they repassivate at E_{rp} . The weld metal exhibited lower resistance to pit growth and was, therefore, more susceptible to pitting compared to the base metal. After aging, repassivation of the base metal was possible but it was much delayed, and E_{rp} was located relatively away from E_{pit} . The aged weld metal was the most susceptible to pitting as there was a significantly higher hindrance in repassivation, and the detrimental effect of σ -phase, in this case, was much more pronounced. Pitting corrosion is controlled by factors related to pit growth stability, which in turn is determined by the maintenance of conditions at the pit surface [41]. Thermal aging had a much higher detrimental impact on resistance to pit growth rather than pit formation. Overall, based on the corrosion studies, it could be summarized that the EB weld metal was more prone to general corrosion and pitting corrosion compared to the base metal. After aging, there was a marked weakening of the base metal against general as well as pitting corrosion. The weld metal's behavior pitting behavior was also similarly affected after aging. However, the exception was in the case of the aged weld metal as its general corrosion behavior was not consistent with its pitting behavior concerning the effect of thermal aging. Thereafter, to confirm the microstructure–corrosion behavior relationship, the specimens were subjected to corrosion tests in a different solution.

Corrosion studies in 0.5 M H_2SO_4 + 0.5 M NaCl solution

Representative LPR test curves along with average values of R_p for the specimens are shown in Fig. 12a. The weld metal showed a lower R_p (68.65 $\text{k}\Omega \text{ cm}^2$) than the base metal (74.84 $\text{k}\Omega \text{ cm}^2$), thus indicating that corrosion resistance of DSS decreased after EB welding. A similar trend of R_p was obtained for these specimens in neutral-chloride solution. There was a slight drop in R_p of the weld metal after aging, thus suggesting a minor loss in corrosion resistance which was different from the LPR results obtained previously. For the base metal, there was an unexpected increase in R_p after aging. The tendency to undergo general corrosion for the weld metal and base metal differed from each other in two different tests

solutions. Further studies were needed to clarify the inconsistency, so EIS tests were conducted.

The results of EIS tests as Nyquist and Bode plots are presented in Fig. 12b and c, respectively. The general profile of the impedance diagrams for all the specimens was the same, thus suggesting that a similar mechanism of charge transfer through the passive oxide layer and across the film/electrolyte interface prevailed. From Nyquist plots, it could be seen that the size of the unfinished semi-circular arc was larger for the base metal compared to the weld metal. In Bode magnitude plots, a higher impedance value was noted in the low-frequency region for the base metal. Furthermore, the base metal also exhibited higher phase shift maxima than the weld metal. These results suggested that the passive film formed on the base metal was relatively more stable and protective towards electrochemical dissolution than the weld metal. There was a notable reduction in arc size of the weld metal after aging, whereas, for the base metal, arc size increased considerably. In Bode magnitude plots, higher impedance was observed in the low-frequency region for aged base metal, while for the weld metal and its aged counterpart, the values were relatively less distinguishable. The phase shift maxima for the aged base metal was noticeably the same as the base metal, whereas, for the weld metal, the phase shift maxima decreased (and was the lowest) after aging. For quantitative interpretation, impedance spectra were fitted to the EEC model used previously, and the results obtained are given in Table 7.

The experimental and simulated spectra (Fig. 12b, c) showed close resemblance, and the very low values of the χ^2 function were suggestive of a good fitting. The values of R_s were nearly the same for all the specimens and were very low compared to R_{ct} values. The weld metal showed lower R_{ct} than the base metal, indicative of its lower corrosion resistance. Furthermore, the value of Q for the weld metal was higher than the base metal, which indicated that the passive oxide film formed on the base metal was relatively thicker [5]. The value of exponent “ n ” decreased after welding which indicated that the weld metal surface heterogeneity was more compared to the base metal, and a relatively more heterogeneous corrosion process occurred in the weld metal [33]. This could be attributed to microstructural phase imbalance in the weld metal. After aging, R_{ct} decreased for the weld metal which

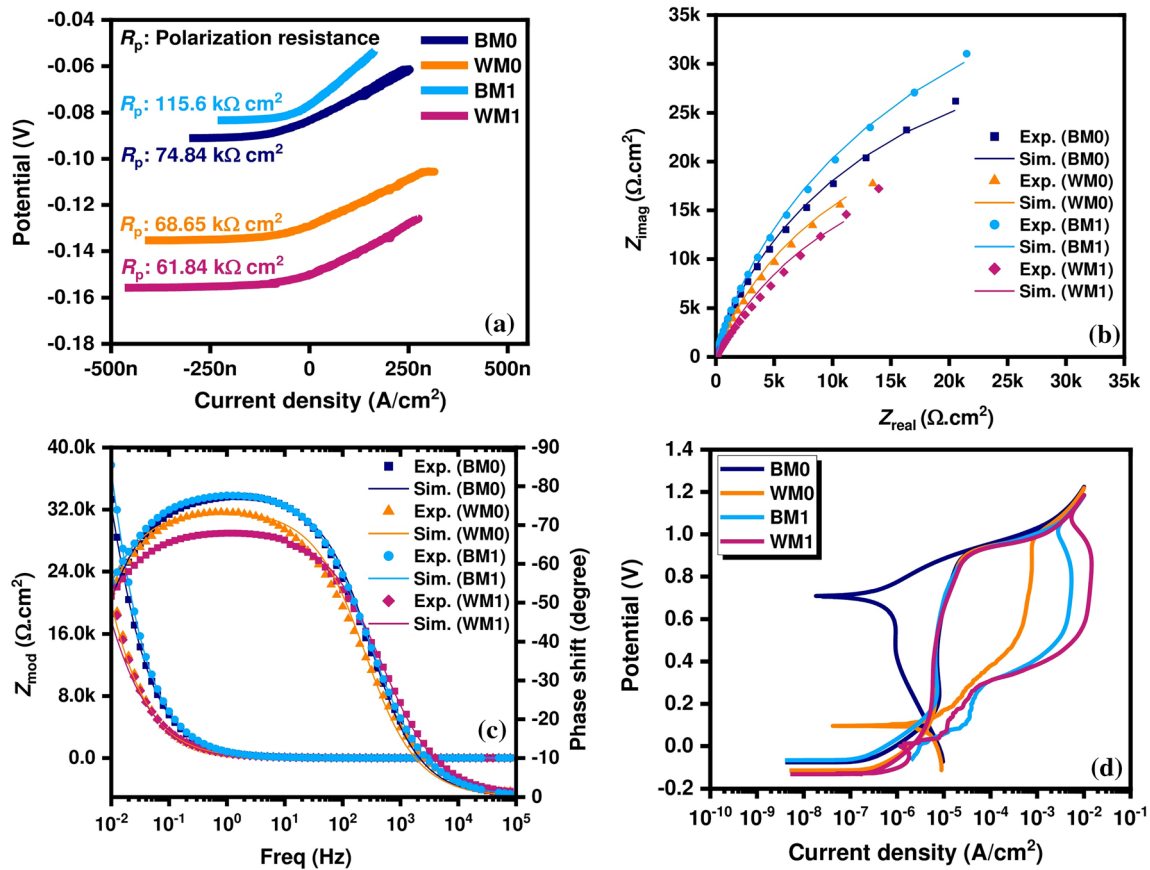


Figure 12 a LPR test curves, b Nyquist plots, c Bode plots, and d CPP scan curves for the specimens tested in 0.5 M H₂SO₄ + 0.5 M NaCl solution.

Table 7 Parameters obtained after fitting the experimental impedance spectra to the equivalent electrical circuit model for different specimens tested in 0.5 M H₂SO₄ + 0.5 M NaCl solution

Specimen	R_s (Ω cm ²)	CPE, Q (Ω^{-1} cm ⁻² s ⁿ)	R_{ct} (Ω cm ²)	n	Goodness of Fit (χ^2)
BM0	$5.546 \pm 26.75e-3$	$265.8e-6 \pm 1.481e-6$	$70.79e3 \pm 2.459e3$	$862.3e-3 \pm 1.377e-3$	1.274×10^{-3}
WM0	$5.606 \pm 26.94e-3$	$422.8e-6 \pm 2.402e-6$	$60.39e3 \pm 3.261e3$	$823.8e-3 \pm 1.471e-3$	4.046×10^{-3}
BM1	$5.636 \pm 31.25e-3$	$247.2e-6 \pm 1.363e-6$	$92.46e3 \pm 3.773e3$	$863.7e-3 \pm 1.362e-3$	808.8×10^{-6}
WM1	$5.504 \pm 28.22e-3$	$396.5e-6 \pm 2.343e-6$	$55.31e3 \pm 3.192e3$	$766.3e-3 \pm 1.404e-3$	3.795×10^{-3}

meant that charge transfer was much easier, indicating a loss in passive film stability of the weld metal. Furthermore, surface heterogeneity was also more in the case of aged weld metal as indicated by the lower value of exponent “n”. It was clear that loss in corrosion resistance of weld metal was caused due to aging. The corrosion behavior of the base metal after aging was however different. The aged base metal showed higher R_{ct} , lower value of Q , and almost equal value of exponent “n” compared to its unaged counterpart. The aged base metal possessed higher corrosion resistance, which was consistent

with the results obtained by LPR tests. However, such a corrosion resistance trend was highly unlikely, keeping in view the detrimental precipitation that was caused in the microstructure of the base metal by aging. Such type of corrosion behavior of the aged base metal was unclear. It is noteworthy that similar results have been reported in the case of DSS aged at 850 °C [42]. Both EIS and LPR techniques depicted a similar trend of corrosion resistance order which indicated that during aging, complex corrosion characteristics were exhibited by DSS.

Pitting corrosion susceptibility of the specimens was evaluated using the CPP test, and their representative curves are shown in Fig. 12d. The data obtained from CPP curves are given in Table 6. The first observation was related to the effect of the test solution on the nature of CPP curves in terms of the anodic polarization process. Irrespective of the microstructure, it was observed that E_{pit} values were decreased when CPP tests were conducted in acidic-chloride solution. The decrease in pH of the test solution shifted the magnitude of E_{pit} to more active values, indicating a detrimental effect on the anodic polarization behavior. Similar to the results obtained in neutral-chloride solution, E_{pit} values in this case also were in a close range. The E_{corr} values for the base metal in both conditions were slightly higher compared to weld metal specimens. Thus, the $E_{\text{pit}} - E_{\text{corr}}$ range was slightly more for the weld metal (Table 6). The results from the forward scan implied that the pitting corrosion resistance was not significantly affected by phase imbalance and σ -phase formation in the microstructure. Similar results have been reported in a study on multipass weld joint of UNS S32750 superduplex stainless steel [43]. The base metal showed excellent behavior against pitting, and its E_{rp} was located above E_{pit} which suggested that it was not susceptible to pitting corrosion. The weld metal, on the other hand, showed E_{pit} comparable to the base metal but its E_{rp} was shifted to much active value which was away from E_{pit} . This implied that the weld metal was characterized by high resistance to pitting corrosion initiation, but once the passive oxide film underwent local breakdown, pit growth stability was high enough to prevent an easy repassivation. The rapid increase in the anodic current density in the passive region could be due to pitting or transpassive dissolution. The examination of the weld metal after the CPP test revealed that it suffered from pitting rather than a transpassive attack. Since the hysteresis loop closed during the reverse scan, it meant that repassivation was possible. However, a very low E_{rp} indicated that the weld metal exhibited poor resistance to pit growth, making it overall susceptible to pitting. The resistance to pit growth (indicated by $E_{\text{pit}} - E_{\text{rp}}$) for the weld metal was affected much adversely when tested in acidic-chloride solution with lower pH, and the repassivation was much more delayed compared to the neutral-chloride solution (Table 6). The resistance to pit growth decreases with the increase in the difference

between E_{pit} and E_{rp} [12]. After aging, the base metal underwent a remarkable loss in its E_{rp} , as the breakdown potential was followed by the formation of a large-sized positive hysteresis loop which did not close during the reverse polarization scan. The increased pitting corrosion susceptibility could be attributed to compositional heterogeneity in the microstructure caused due to aging-induced precipitates which were responsible for hindering the repassivation process. The weld metal after aging also showed a loss in E_{rp} and exhibited a large hysteresis loop similar to the aged base metal, but the loop closed during the reverse scan in this case. Repassivation was possible but it was significantly delayed. It showed lower resistance to pit growth compared to the as-welded specimen. The bigger size of the hysteresis loop implies more passive film disruption, followed by more difficulty in restoring the damaged passive film [37]. The key observation from these results was that using the CPP test, the pitting corrosion behavior of the specimens with marked microstructural differences could be understood, and as such, the superiority of the CPP test over the PAP test was revealed. Therefore, it could be deduced that the determination of both E_{pit} , as well as E_{rp} , is crucial for reliable pitting corrosion behavior assessment of DSS after welding or thermal aging.

Overall, based on the corrosion studies in two different test solutions, the effect of EB weld thermal cycle on the general and pitting corrosion behavior of DSS base metal, and the influence of aging on the localized corrosion behavior of the weld metal and base metal could be understood. However, given the inconsistent trend observed for the aged weld metal and base metal concerning their general corrosion tendency in two different test solutions, further studies are required to get insights into their passive film characteristics.

Characterization of localized corrosion

The specimens after CPP testing in acidic-chloride solution were subjected to SEM examination. SEM images of the region near top and bottom of the weld metal are presented in Fig. 13a and b, respectively. The region near weld top was noticeably free from any localized corrosion attack. The corrosion pits were mainly located towards bottom or root region of the weld. Pits were observed at distinct locations as well as there were regions where multiple pits

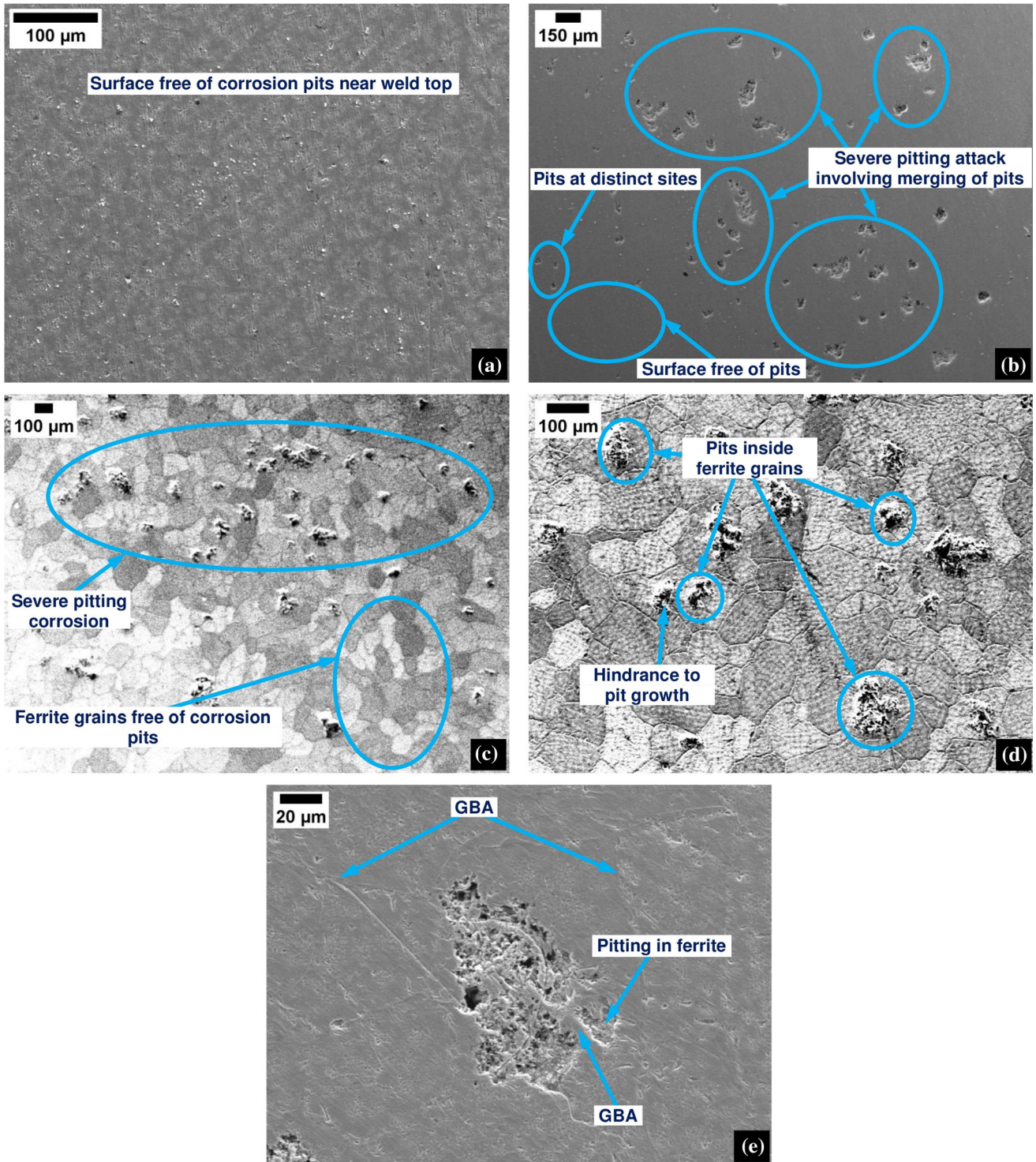


Figure 13 SEM images of the weld metal specimen (as-welded condition) after CPP testing: **a, b** near weld top and bottom, respectively without etching, and **c–e** near weld bottom after etching at $\times 43$, $\times 100$, and $\times 500$ magnifications, respectively.

merged, as a result of poor resistance of the weld metal to pit growth. There were some regions devoid of corrosion pits, whereas, in some adjacent regions, pitting was rather severe (Fig. 13b).

These observations suggested that weld top region was relatively more pitting-resistant than bottom region. Such a difference in corrosion resistance could be correlated to the through-thickness

microstructural differences between top and bottom regions. The higher austenite content in the microstructure of weld top region (Fig. 5a–c) accounted for its relatively better pitting corrosion resistance than weld bottom region (Fig. 5d–f). To identify the weaker phase and regions in the weld metal where pitting occurred preferentially, the specimen was etched to reveal its microstructure. Figure 13c shows the low-magnification SEM image taken near bottom region of the weld metal. The microstructure was predominantly ferritic with signs of selective pitting attack in some regions, while there were regions in which ferrite grains were completely free of pits. A relatively higher magnification microscopic observation (Fig. 13d) revealed that pitting occurred predominantly within ferrite grains. For most of the regions, pitting initiation occurred intragranularly and the growth of pits consumed a significant portion of ferrite grains. Moreover, at a few sites, α/γ interfacial regions were also affected due to pitting. The regions within ferrite grains where probably IGA precipitates were present could provide hindrance in the propagation of corrosion pits as depicted in Fig. 13d. This deduction is supported by the results reported by Han et al. [44], who observed that fine-grained IGA was beneficial in improving the stability and continuity of the passive film in DSS weld metal. The corroded weld metal was further examined at a relatively higher magnification (Fig. 13e). It could be seen that pitting prone regions were mainly within the ferrite phase while grain boundary austenite appeared unaffected, thus indicating that austenite was the more corrosion-resistant phase [10]. The key finding from corrosion behavior analysis of the EB weld metal was that the high pitting susceptibility of the weld metal was mainly due to its weaker root region in terms of higher ferrite content (hence lower austenite proportion) and a higher propensity to precipitation of Cr-nitrides [11, 12]. Microstructural heterogeneity was observed in the weld metal in a manner that overall austenite content was higher near weld top region compared to bottom region. Due to the rapid cooling rates associated with the thermal cycle of EBW, the primary precipitates deleterious to localized corrosion resistance are the Cr-nitrides [11, 23]. Similar to the present results, Westin et al. [45] observed the preferential pitting of the highly ferritic root side of a single-pass DSS weld in the ASTM G48-E corrosion test.

Heat input is one of the key variables which influences the cooling rate after welding, and consequently affects microstructural phase transformations and corrosion resistance. Effect of heat input in welding of DSS has been reported in different works involving different welding processes. In a study on GTA-welded UNS S32906 super-DSS, out of three heat input levels (1.19, 1.46, 1.87 kJ/mm) investigated, high heat input was reported to be deliver best weld properties attributable to favorable microstructural formation [46]. Another study on shielded metal arc (SMA)-welded austenitic-ferritic DSS did not reveal any clear trend between corrosion resistance and heat input levels (0.4, 0.8, 1.1, and 1.6 kJ/mm) [47]. Further, a study on keyhole GTA-welded 2205 DSS using three heat input levels (1.57, 1.74, and 1.94 kJ/mm) reported an increase of austenite proportion with an increase in heat input, however, there was no significant variation in E_{pit} of weld metals owing to their similar chemical composition [44]. An investigation on studying the influence of varying heat input (0.43, 0.46, and 0.50 kJ/mm) in EB-welded DSS indicated that the effects of change in heat input on microstructure and pitting corrosion resistance were limited [11]. Finally, a study on pulsed current GTA-welded UNS S32760 SDSS using four levels of heat input (0.63, 0.76, 0.95, and 1.12 kJ/mm) highlighted the key roleplay of heat input in affecting microstructure and corrosion resistance [48]. Overall, the relationship between heat input level and corrosion resistance of DSS welds is far from simplistic, and the microstructural characteristics have the most important roleplay in deciding the suitability of welds for actual service environments.

For a better understanding of the microstructural dependence of pitting corrosion resistance in the present work, a schematic illustration of microstructural heterogeneity in the weld metal and its effect on the pitting behavior of EB-welded DSS is presented in Fig. 14a–d. From the transverse section of the weld joint (Fig. 14a), it could be seen that there was a gradual variation in the weld width from top to bottom region. Due to the variation in the weld volume, microstructural differences existed between top and bottom regions (Fig. 14b). The region near the upper surface cools relatively slowly, and therefore microstructure in this region exhibited a higher austenite proportion compared to bottom region of the weld (Fig. 14c).

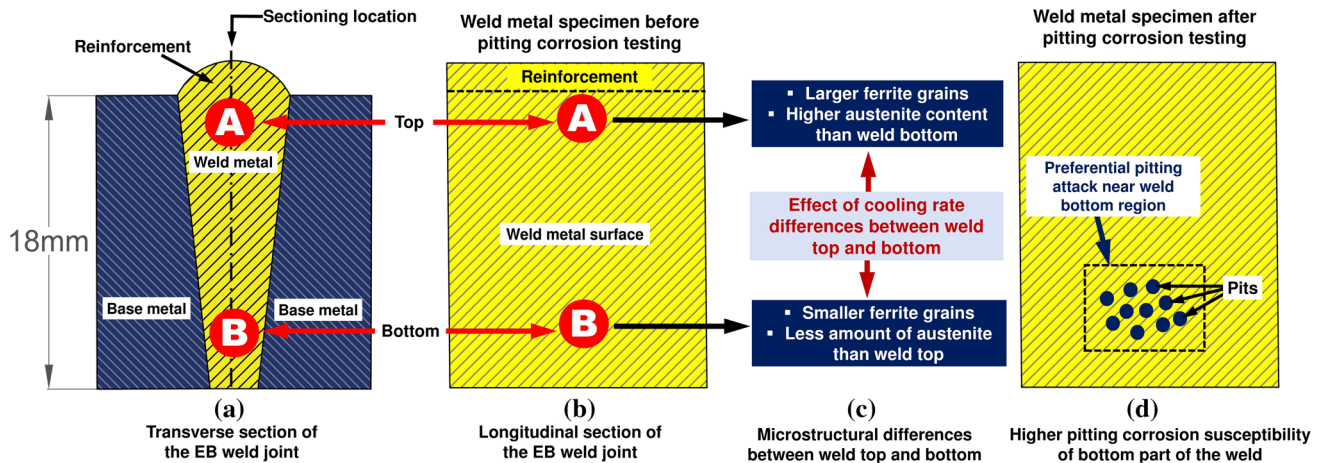


Figure 14 Schematic illustration of through-thickness microstructural heterogeneity in DSS EB welded joint and its effect on pitting corrosion resistance property.

Due to the expectedly faster cooling rate near bottom region, the tendency of Cr-nitride precipitation was more [25]. It was revealed that pitting occurred preferentially near bottom region of the weld as discussed previously, and as schematically illustrated in Fig. 14d. Due to lower austenite content and expectedly higher cooling rate, Cr-nitride precipitation probably occurred towards bottom region of the weld as a result of which it was more prone to pitting corrosion. There is a certain width of the Cr-depleted zone on the phase boundaries between Cr-nitrides and ferrite, as a result of which the continuity of the passive film could be damaged in the ferrite [44]. From a practical application viewpoint, the present results suggested that in the case of thick-section DSS welds produced using the EBW process, the bottom/root region could be the potential site where preferential pitting corrosion attack might take place as a result of its unfavorable microstructure. Considering this, such types of welds might not be suitable for applications in service environments where there is a risk of localized corrosion attack. Therefore, microstructural control in bottom/root region of EB DSS welds during the fabrication stage is crucial.

Figure 15a shows the SEM image of the aged weld metal after the CPP test before etching. The pitting morphology was noticeably different when compared to its as-welded counterpart. Figure 15b and c shows the micrographs of regions near weld top and bottom, respectively, after etching. As discussed in the CPP test results, the weld metal in both conditions possessed poor resistance to pit growth. In the aged weld metal, there was a severe pitting attack

throughout the whole surface exposed to the test solution, unlike its as-welded counterpart. Both top and bottom regions showed widespread corrosion pits covering a large surface area. The presence of clustered morphology indicated that pit growth was predominant, and σ -phase precipitation led to the creation of more pitting susceptible sites in the weld metal microstructure. The elongated pit geometry observed in the aged weld metal could have resulted due to the activation of secondary pitting in the regions close to the initial pit formation site [40]. The occurrence of pitting in the aged weld metal could be attributed to aging-induced σ -phase precipitation [2, 6]. The transformation reaction of eutectoid decomposition of ferrite results in σ -phase and secondary austenite. The main ferrite forming elements, viz., Cr and Mo migrate to σ -phase and therefore, the composition of newly formed austenite is poorer in these elements, as a consequence of which it exhibits lower corrosion resistance [2, 26]. Comparing the morphology of corrosion pits on the weld metal in different conditions (Figs. 13b–d and 15a–c), it was observed that for the as-welded specimen, corrosion pits possessed noticeably higher depth compared to pits observed on the aged specimen. The surface area affected due to pitting, however, was relatively more for the aged weld metal. It was noteworthy that the occurrence of such corrosion pits was predominantly near weld bottom region only in the as-welded condition, whereas pits were widespread throughout the area exposed to the test solution in the case of aged weld metal. These observations indicated that the pit nucleation sites were more in the aged weld metal.

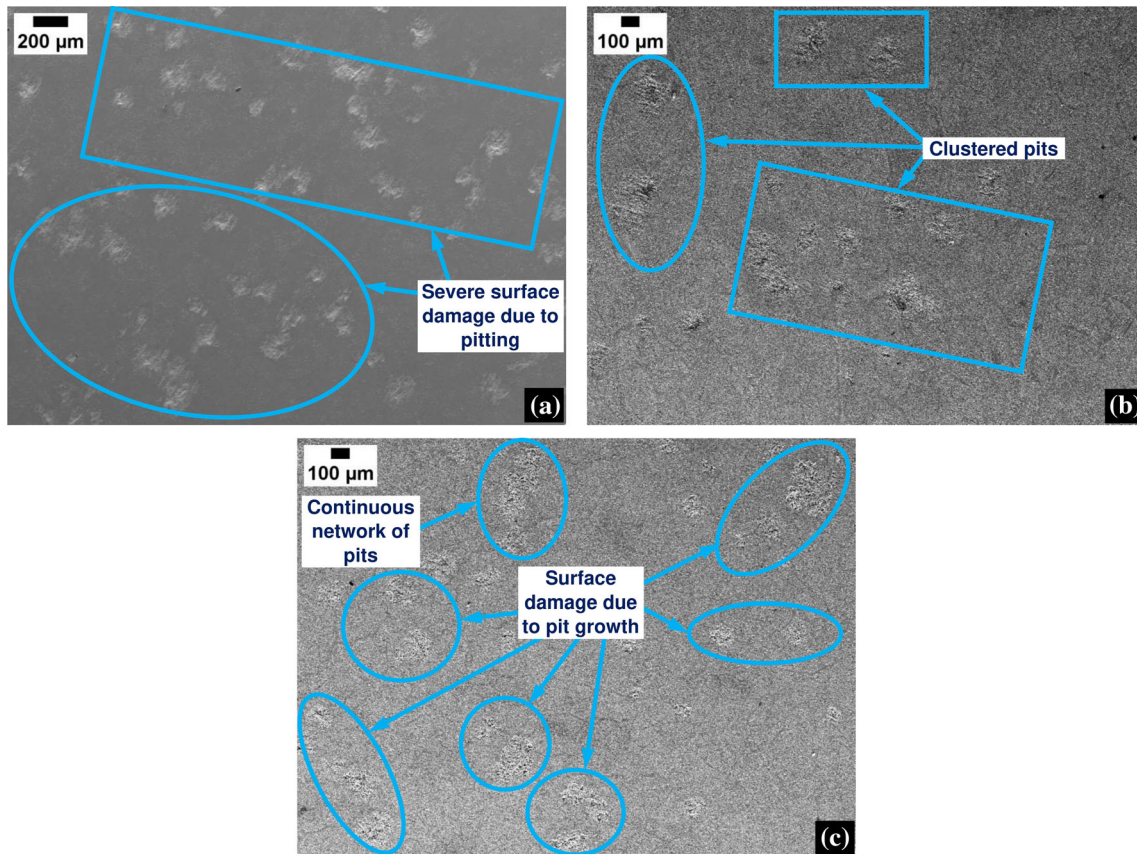


Figure 15 SEM images of the weld metal specimen in the aged condition after CPP testing **a** before chemical etching (at $\times 37$), **b** region near weld top after etching (at $\times 40$), and **c** region near weld bottom after etching (at $\times 40$).

Conclusions

In the present work, the corrosion (general and pitting) behavior of exclusively the weld metal/fusion zone of 2205 duplex stainless steel (DSS) electron beam (EB) welded joint was studied in neutral-chloride and acidic-chloride test solutions, supported by microstructural investigations. The effect of thermal aging (850 °C/2 h) on microstructure and corrosion behavior of weld metal and base metal was also studied. The main outcomes of the present study are summarized below:

1. The weld metal microstructure was characterized by phase imbalance containing a higher ferrite proportion compared to austenite.
2. Microstructural heterogeneity was observed in the weld metal in a manner that austenite formation was relatively more near weld top region compared to bottom region.
3. The effect of aging-induced precipitation was indicated by the reduction in ferrite content of

both weld metal and base metal. The microstructures of the weld metal and base metal in the aged condition were characterized by a significant compositional heterogeneity as indicated by SEM/EDS results.

4. The formation of intermetallic σ -phase in the aged weld metal as evidenced through XRD analysis could be correlated to the ferrite phase being getting consumed as indicated by a significant reduction in the ferrite content under the aged condition.
5. The weld metal showed a relatively higher general and pitting corrosion tendency compared to the base metal. Further, the susceptibility of the weld metal to pitting corrosion was mainly due to the weaker bottom region of the weld due to its unfavorable microstructure.
6. Detrimental effect of σ -phase precipitation was revealed by markedly decreased resistance to pit growth and hindrance to repassivation process,

as a result of which the weld metal, as well as base metal, became more prone to pitting.

7. For a reliable assessment of pitting corrosion behavior of DSS, it is recommended to determine both E_{pit} and E_{rp} , than E_{pit} alone.
8. In general, this study revealed about unfavorable microstructural formation near bottom region of the weld zone and its detrimental effect in rendering thick section autogenous EB DSS welds susceptible to pitting corrosion.

Acknowledgements

The infrastructural support in the form of testing facilities provided by Welding Metallurgy Laboratory (Department of Mechanical Engineering), and Central Facility, SLIET, Longowal, is gratefully acknowledged.

Declarations

Conflict of interest The authors declare that they have no conflict of interest.

References

- [1] International Molybdenum Association (2014) Practical guidelines for the fabrication of duplex stainless steel, 3rd edn. International Molybdenum Association, London
- [2] Fargas G, Anglada M, Mateo A (2009) Effect of the annealing temperature on the mechanical properties, formability and corrosion resistance of hot-rolled duplex stainless steel. *J Mater Process Technol* 209:1770–1782
- [3] Singh S, Singh J, Shahi AS (2020) Investigation on aging-induced degradation of impact toughness and corrosion performance of duplex stainless steel weldment. *Trans Ind Inst Metal* 73(11):2747–2765
- [4] Azevedo CRF, Pereira HB, Wolyneć S, Padilha AF (2019) An overview of the recurrent failures of duplex stainless steels. *Eng Fail Anal* 97:161–188
- [5] Xie Y, Guo S, Leong A, Zhang J, Zhu Y (2017) Corrosion behaviour of stainless steel exposed to highly concentrated chloride solutions. *Corros Eng Sci Tech* 52(4):283–293
- [6] Potgieter JH (1992) Influence of σ phase on general and pitting corrosion resistance of SAF 2205 duplex stainless steel. *Br Corros J* 27(3):219–223
- [7] Yan HT, Xin SS, Yang Y, Yang S, Li MC (2019) Electrochemical corrosion behavior of 2205 duplex stainless steel welds in chloride solutions. *Int J Electrochem Sci* 14:1423–1433
- [8] Zhang Z, Jing H, Xu L, Han Y, Zhao L (2016) Investigation on microstructure evolution and properties of duplex stainless steel joint multi-pass welded by using different methods. *Mater Des* 109:670–685
- [9] Shi Y, Cui S, Zhu T, Gu S, Shen X (2018) Microstructure and intergranular corrosion behavior of HAZ in DP-TIG welded DSS joints. *J Mater Process Technol* 256:254–261
- [10] Yang Y, Wang Z, Tan H, Hong J, Jiang Y, Jiang L, Li J (2012) Effect of a brief post-weld heat treatment on the microstructure evolution and pitting corrosion of laser beam welded UNS S31803 duplex stainless steel. *Corros Sci* 65:472–480
- [11] Zhang Z, Jing H, Xu L, Han Y, Zhao L, Lv X, Zhang J (2018) Influence of heat input in electron beam process on microstructure and properties of duplex stainless steel welded interface. *Appl Surf Sci* 435:352–366
- [12] Singh J, Shahi AS (2021) Electrochemical corrosion behavior and microstructural characteristics of electron beam welded UNS S32205 duplex stainless steel. *Mater Corros* 72(8):1350–1369
- [13] Singh J, Shahi AS (2020) Metallurgical and corrosion characterization of electron beam welded duplex stainless steel joints. *J Manuf Process* 50:581–595
- [14] Zeng H, Yang Y, Xu R, Xin S, Li M (2019) Pitting corrosion resistance of sensitized type 2205 duplex stainless steel in hot concentrated seawater. *J Solid State Electrochem* 23:2793–2801
- [15] Magnabosco R (2009) Kinetics of sigma phase formation in a duplex stainless steel. *Mater Res* 12(3):321–327
- [16] Yongqiang W, Hao S, Na L, Yanhao X, Hemin J (2018) Effect of sigma phase precipitation on the pitting corrosion mechanism of duplex stainless steels. *Int J Electrochem Sci* 13:9868–9887
- [17] Pan J (2020) Studying the passivity and breakdown of duplex stainless steels at micrometer and nanometer scales—the influence of microstructure. *Front Mater* 7:133
- [18] Li J, Du CW, Liu ZY, Li XG, Liu M (2018) Effect of microstructure on the corrosion resistance of 2205 duplex stainless steel. Part 1: Microstructure evolution during isothermal aging at 850°C and evaluation of anticorrosion properties by methods of cyclic potentiodynamic polarization and electrochemical impedance tests. *Constr Build Mater* 189:1286–1293
- [19] Kang DH, Lee HW (2013) Study of the correlation between pitting corrosion and the component ratio of the dual phase in duplex stainless steel welds. *Corros Sci* 74:396–407

- [20] Krizan D, Duprez L, De Cooman BC (2004) Properties of laser welded SAF 2205 duplex stainless steel sheet. *Steel Res Int* 75(12):829–835
- [21] Cui S, Pang S, Pang D, Zhang Z (2021) Influence of welding speeds on the morphology, mechanical properties, and microstructure of 2205 DSS welded joint by K-TIG welding. *Materials* 14:3426
- [22] Xie X, Li J, Jiang W, Dong Z, Tu ST, Zhai X, Zhao X (2020) Nonhomogeneous microstructure formation and its role on tensile and fatigue performance of duplex stainless steel 2205 multi-pass weld joints. *Mater Sci Eng A* 786:139426
- [23] Krasnorutskiy S, Kipp C, Hensel J, Kaestner P, Hartwig S, Bräuer G, Dilger K (2018) Metallurgical investigation of electron beam welded duplex stainless steel X2CrNiMoN22-5-3 with plasma nitrided weld edge surfaces. *Mater Test* 60:577–582
- [24] Xia X, Wu J, Liu Z, Ji H, Shen X, Ma J, Zhuang P (2019) Correlation between microstructure evolution and mechanical properties of 50 mm 316L electron beam welds. *Fusion Eng Des* 147:111245
- [25] Karlsson L, Arcini H (2012) Low energy input welding of duplex stainless steels. *Weld World* 56:41–47
- [26] Calliari I, Zanesco M, Ramous E (2006) Influence of isothermal aging on secondary phases precipitation and toughness of a duplex stainless steel SAF 2205. *J Mater Sci* 41:7643–7649
- [27] Stergiou V, Papadimitriou GD (2012) Effect of an electron beam surface treatment on the microstructure and mechanical properties of SAF 2205 joints produced with electron beam welding. *J Mater Sci* 47:2110–2121
- [28] Singh J, Shahi AS (2019) Metallurgical, impact and fatigue performance of electron beam welded duplex stainless steel joints. *J Mater Process Technol* 272:137–148
- [29] Silva DDS, Simões TA, Macedo DA, Bueno AHS, Torres SM, Gomes RM (2021) Microstructural influence of sigma phase on pitting corrosion behavior of duplex stainless steel/NaCl electrolyte couple. *Mater Chem Phys* 259:124056
- [30] Radojković B, Kovačina J, Jegdić B, Bobić B, Alić B, Marunčić D, Simović A (2021) Influence of inhibitors on the corrosion behavior of the X5CrNi1810 stainless steel-welded joint. *Mater Corros* 72(4):694–707
- [31] Mirshekari GR, Tavakoli E, Atapour M, Sadeghian B (2014) Microstructure and corrosion behavior of multipass gas tungsten arc welded 304L stainless steel. *Mater Des* 55:905–911
- [32] An JH, Lee J, Kim YS, Kim WC, Kim JG (2019) Effects of Post weld heat treatment on mechanical and electrochemical properties of welded carbon steel pipe. *Met Mater Int* 25:304–312
- [33] Kakaei K, Esrafil MD, Ehsani A (2019) Graphene and anticorrosive properties, in Kakaei K, Esrafil MD, Ehsani A (Eds.). *Interface Sci Technol* 27:303–337
- [34] Sinhmar S, Dwivedi DK (2018) A study on corrosion behavior of friction stir welded and tungsten inert gas welded AA2014 aluminium alloy. *Corros Sci* 133:25–35
- [35] Derakhshi MA, Kangazian J, Shamanian M (2019) Electron beam welding of Inconel 617 to AISI 310: corrosion behavior of weld metal. *Vacuum* 161:371–374
- [36] Jegdić BV, Bobić BM, Radojković BM, Alić B (2019) Influence of welding parameters on pit initiation and pit growth in welded joints of X5CrNi18-10 stainless steel. *Weld World* 63:167–179
- [37] Esmailzadeh S, Aliofkhaezrai M, Sarlak H (2018) Interpretation of cyclic potentiodynamic polarization test results for study of corrosion behavior of metals: a review. *Prot Met Phys Chem* 54(5):976–989
- [38] He L, Wirian L, Singh PM (2019) Effects of isothermal aging on the microstructure evolution and pitting corrosion resistance of lean duplex stainless steel UNS S32003. *Metall Mater Trans A* 50A:2103–2113
- [39] Sicupira DC, Frankel GS, Lins VFC (2016) Pitting corrosion of welds in UNS S32304 lean duplex stainless steel. *Mater Corros* 67(5):440–448
- [40] Razavi RS (2016) Laser beam welding of Waspaloy: characterization and corrosion behavior evaluation. *Opt Laser Technol* 82:113–120
- [41] Frankel GS (1998) Pitting corrosion of metals, a review of the critical factors. *J Electrochem Soc* 145(6):2186–2198
- [42] Chaves R, Costa I, Melo HGD, Wolyneć S (2006) Evaluation of selective corrosion in UNS S31803 duplex stainless steel with electrochemical impedance spectroscopy. *Electrochim Acta* 51:1842–1846
- [43] Tavares SSM, Pardal JM, Lima LD, Bastos IN, Nascimento AM, de Souza JA (2007) Characterization of microstructure, chemical composition, corrosion resistance and toughness of a multipass weld joint of superduplex stainless steel UNS S32750. *Mater Charact* 58:610–616
- [44] Han L, Han T, Chen G, Wang B, Sun J, Wang Y (2021) Influence of heat input on microstructure, hardness and pitting corrosion of weld metal in duplex stainless steel welded by keyhole-TIG. *Mater Charact* 175:111052
- [45] Westin EM, Stelling K, Gumenyuk A (2011) Single-pass laser-GMA hybrid welding of 13.5 mm thick duplex stainless steel. *Weld World* 55:39–49
- [46] Vahman M, Shamanian M, Golozar MA, Jalali A, Sarmadi MA, Kangazian J (2020) The effect of welding heat input on the structure–property relationship of a new grade super duplex stainless steel. *Steel Res Int* 91:1900347

- [47] Jana S (1992) Effect of heat input on the HAZ properties of two duplex stainless steels. *J Mater Process Technol* 33:247–261
- [48] Yousefieh M, Shamanian M, Saatchi A (2011) Influence of heat input in pulsed current GTAW process on

microstructure and corrosion resistance of duplex stainless steel welds. *J Iron Steel Res Int* 18:65–69

Publisher's Note Springer Nature remains neutral with regard to jurisdictional claims in published maps and institutional affiliations.